# The generic nature of the tropospheric response to sudden stratospheric warmings

Ian White*

*The Hebrew University of Jerusalem, Institute of Earth Sciences, Edmond J. Safra Campus, Givat Ram, Jerusalem, Israel*

Chaim I. Garfinkel

*The Hebrew University of Jerusalem, Institute of Earth Sciences, Edmond J. Safra Campus, Givat Ram, Jerusalem, Israel*

Edwin P. Gerber

*Courant Institute of Mathematical Sciences, New York University, New York, USA*

Martin Jucker

*Climate Change Research Centre, University of New South Wales, Sydney, Australia*

Peter Hitchcock

*Department of Earth and Atmospheric Sciences, Cornell University, New York, USA*

Jian Rao

*The Hebrew University of Jerusalem, Institute of Earth Sciences, Edmond J. Safra Campus, Givat Ram, Jerusalem, Israel*

*Corresponding author address:* Ian White, The Hebrew University of Jerusalem, Institute of Earth Sciences, Edmond J. Safra Campus, Givat Ram, Jerusalem, Israel.

E-mail: ian.white@mail.huji.ac.il

ABSTRACT

The tropospheric response to mid-winter sudden stratospheric warmings (SSWs) is examined using an idealised model. SSW events are triggered by imposing high-latitude stratospheric heating perturbations of varying magnitude for only a few days, spun-off from a free-running control integration (CTRL). The evolution of the thermally-triggered SSWs are then compared with naturally-occurring SSWs identified in CTRL. By applying a heating perturbation, with no modification to the momentum budget, it is possible to isolate the tropospheric response directly attributable to a change in the stratospheric polar vortex, independent of any planetary-wave momentum torques involved in the initiation of a SSW.

Zonal-wind anomalies associated with the thermally-triggered SSWs first propagate downward to the high-latitude troposphere after $\sim 2$ weeks, before migrating equatorward and stalling at midlatitudes, where they straddle the near-surface jet. After $\sim 3$ weeks, the circulation and eddy fluxes associated with thermally-triggered SSWs, evolve very similarly to SSWs in CTRL, despite the lack of initial planetary-wave driving. This suggests that at longer lags, the tropospheric response to SSWs is generic and governed by the strength of the lower-stratospheric warming, whereas at shorter lags, the initial formation of the SSW potentially plays a large role in the downward coupling.

In agreement with previous studies, synoptic waves are found to play a key role in the persistent tropospheric jet shift at long lags. Synoptic waves appear to respond to the enhanced midlatitude baroclinicity associated with the tropospheric jet shift, and preferentially propagate poleward in an apparent positive feedback with changes in the high-latitude refractive index.

## 1. Introduction

A change in the strength of the stratospheric polar vortex can have an appreciable influence on the position of the tropospheric midlatitude eddy-driven jet (e.g., Baldwin and Dunkerton 2001; Polvani and Kushner 2002; Kidston et al. 2015). In particular, there is considerable evidence in observations and models that a weakening of the polar vortex gives rise to a persistent equatorward shift of the lower-tropospheric jet. One of the most striking examples of this downward coupling occurs during a sudden stratospheric warming (SSW), wherein the polar vortex weakens and warms in the space of a few days (Scherhag 1952). Following an SSW, the equatorward tropospheric jet shift can persist for four or more weeks; substantially longer than the tropospheric decorrelation timescale in the absence of such an event (e.g., Baldwin and Dunkerton 2001; Gerber et al. 2010; Simpson et al. 2011). Extreme vortex events such as SSWs can thus provide a potential source of skill for extratropical weather forecasts on subseasonal to seasonal timescales (e.g., Sigmond et al. 2013).

It is implicit in a number of studies that the tropospheric response to SSWs can be separated into two approximate stages: 1) the mechanism by which the stratospheric anomalies are initially communicated downward to the troposphere, and 2) the subsequent amplification and persistence of the tropospheric jet shift (e.g., Song and Robinson 2004; Thompson et al. 2006). In terms of the former, the mechanisms are not well understood and many have been proposed, including ’downward control’ via the wave-induced zonally-symmetric meridional circulation (Haynes et al. 1991; Thompson et al. 2006), a balanced nonlocal response to a stratospheric potential vorticity anomaly (Hartley et al. 1998; Ambaum and Hoskins 2002; Black and McDaniel 2004), as well as changes in planetary-wave propagation, breaking and reflection either directly or indirectly in both the stratosphere and troposphere (e.g., Matsuno 1971; Chen and Robinson 1992; Perlwitz and Harnik 2003; Shaw et al. 2010; Hitchcock and Haynes 2016; Hitchcock and Simpson 2016; Smith and Scott 2016).

To explain the second stage (i.e., the persistent jet shift at longer lags), the general consensus is that synoptic-wave feedbacks are necessary (Limpasuvan et al. 2004; Kushner and Polvani 2004; Song and Robinson 2004; Garfinkel et al. 2013; Hitchcock and Simpson 2014). Indeed, Domeisen et al. (2013) employed a dry dynamical core, to show that in the absence of synoptic-wave feedbacks in the troposphere, the tropospheric response to an SSW would be a poleward-shifted jet, opposite to what is observed. To our knowledge, no study has explicitly tried to separate the short- and long-lag response. It is the latter upon which we focus in this study.

In order to understand how changes in stratospheric temperature (such as those found during a SSW), influence the troposphere, many studies have imposed temperature perturbations to the stratosphere (e.g., Williams 2006; Lorenz and DeWeaver 2007). For instance, Polvani and Kushner (2002) and Kushner and Polvani (2004) developed a modification of the Held and Suarez (1994) forcing where tropospheric and stratospheric temperatures were relaxed to a chosen equilibrium state, to explore the impact of a high-latitude cooling on the troposphere. They demonstrated that the tropospheric response to a colder (stronger) polar vortex is a poleward-shifted jet stream. However, as they also relaxed the tropospheric temperatures, the downward impact was very sensitive to the details of the tropospheric climatology (e.g., Gerber and Polvani 2009). In fact, the magnitude of the tropospheric response to an identical stratospheric perturbation can differ by more than a factor of three depending on the tropospheric state (Garfinkel et al. 2013).

In another set of experiments, Haigh et al. (2005) and Simpson et al. (2009) imposed a steady stratospheric warming at high latitudes and found an equatorward tropospheric jet shift (although the main aim of their work was to understand the tropospheric response to tropical stratospheric warming). All of these studies found that changes in tropospheric eddy momentum fluxes and their feedbacks with the tropospheric circulation, are crucial for the obtained response. Further, Simpson et al. (2009) found that the changes in the quasi-geostrophic refractive index (Matsuno 1970) could explain the tropospheric eddy changes.

While many studies have imposed thermal perturbations to the stratosphere to explore changes in stratospheric variability (see also work by Taguchi et al. 2001; Jucker et al. 2013), the focus has been on the climatological (steady or seasonally-evolving) modifications by applying the heating continuously. As SSWs are associated with a sudden onset of a high-latitude warming, we take a novel approach in this study by imposing a warming for only a few days to initiate a SSW, before switching it off and examining the coupled stratosphere-troposphere response. To do this, we perform a number of integrations with varying-magnitude heating profiles, using the Model of an Idealised Moist Atmosphere (MiMA; Jucker and Gerber 2017) and compare the evolution of the forced SSWs with SSWs taken from a free-running control integration.

By triggering an SSW using a heating perturbation rather than by a modulation of the momentum budget, our experiments allow us to explicitly isolate the part of the downward influence that is attributable to changes in the polar vortex (e.g., subsequent changes in planetary- and synoptic-wave propagation in response to the weakened vortex), as opposed to the downward influence that is associated with the preceding planetary-wave activity which drives a naturally-occurring SSW, or with tropospheric precursors (as found to be important by a number of studies, e.g., Black and

McDaniel 2004; Nakagawa and Yamazaki 2006; Karpechko et al. 2017; White et al. 2019).

Indeed, Plumb and Semeniuk (2003) found that upward-propagating planetary waves emanating from the troposphere can drive wind anomalies at successively lower levels akin to that observed during SSWs. In this case the downward migration occurs as a passive response to upward-propagating waves, such that downward migration during SSWs does not necessarily indicate any stratospheric influence on the troposphere. We will show that the tropospheric response to SSWs at longer lags is somewhat generic, insomuch that the evolution during the thermally-triggered SSWs and the free-running SSWs (i.e., those initiated by momentum torques) are almost indistinguishable. We conclude that the persistent equatorward shift of the tropospheric jet at longer lags is independent of the wave fluxes that force an SSW, and that there is a genuine downward propagation of anomalies from the stratosphere (e.g., Hitchcock and Haynes 2016).

Section 2 provides a description of our model and experiments. Section 3 presents the results of our study, comparing SSWs in a free-running control integration (which are necessarily forced by momentum torques) with those which are thermally triggered. Finally, in Section 4, a summary and discussion is provided.

## 2. Model and Experimental Setup

In this study we utilise a recently-developed Model of an Idealised Moist Atmosphere (referred to hereafter as MiMA; Jucker and Gerber 2017). The most important features of MiMA that distinguish it from dry dynamical cores used in the studies aforementioned, are its explicit treatment of moisture and radiation. These two features are important for simulating a realistic stratosphere and hence for stratosphere-troposphere coupling, which is the focus of this study.

### *a. Model of an Idealised Moist Atmosphere (MiMA)*

MiMA is an intermediate complexity atmospheric model with a dynamical core which has a variety of other well-motivated physical processes. Following Frierson et al. (2006), it iincludes a representation of large-scale moisture transport, latent heat release, a mixed-layer ocean, a subgrid-scale convection scheme (Betts 1986; Betts and Miller 1986), and a Monin-Obukhov similarity boundary-layer scheme. Also incorporated is a more realistic representation of radiation, namely the Rapid Radiative Transfer Model (RRTM) radiation scheme (Mlawer et al. 1997; Iacono et al. 2000), which replaces the grey-radiation scheme of Frierson et al. (2006). The RRTM scheme allows for representation of the radiative impacts of both ozone and water vapour.

Neither a sponge-layer nor Rayleigh damping scheme is utilised; instead, the gravity-wave scheme of Alexander and Dunkerton (1999) is used to represent gravity-wave momentum deposition, following Cohen et al. (2014). The gravity-wave scheme is also modified to ensure that any gravity-wave momentum fluxes which do reach close to the model lid, are deposited in the top three layers so as to avoid possible sponge-layer feedbacks and spurious meridional circulations associated with imposing heating perturbations (Shepherd et al. 1996; Shepherd and Shaw 2004). Full details regarding the model can be found in Jucker and Gerber (2017).

In order to generate a relatively realistic climatology (see figure 1 in the supplementary material) on which our runs will be based, a number of parameters have been updated from the original version provided by Jucker and Gerber (2017). We follow Garfinkel et al. (2019), who modified the lower-boundary conditions of the model to generate as realistic a stationary wave pattern as possible. There are differences between our study and theirs and these are documented in section 1 of the supplementary material, although these differences do not affect our results quantitatively. Another important difference from Jucker and Gerber (2017) and Garfinkel et al. (2019) is the use of a monthly-climatology zonal-mean input ozone file, taken from the pre-industrial era CMIP5 forcing. The SSW frequency is sensitive to the ozone climatology; in particular, if an annual-mean ozone climatology is used, the SSW frequency is higher than if a monthly-varying climatology is used. We refer readers to Garfinkel et al. (2019) for details on the exact model setup.

*b. Experimental Setup*

A series of runs are performed at T42 horizontal resolution (2.8°x2.8°) and with 40 vertical levels spanning the surface to $\sim$ 0.01 hPa (i.e., close to 70km). We start by running the model freely for 50 years after discarding the first 10 years to allow the mixed-layer ocean to reach an equilibrium state. This 50-year control integration is herein referred to as the CTRL run. Following

In CTRL, 22 SSWs are found using the WMO criterion (McInturff 1978) that the zonal-mean zonal wind at 60°N and 10 hPa must reverse, along with the extra conditions that the SSW must occur during November to April, returning to westerly winds for at least 10 consecutive days (to avoid counting final warmings), and that no two consecutive SSW events can occur within 20 days of one another (to ensure that events are distinct; following Charlton and Polvani 2007). The ratio of SSWs in CTRL is 0.44 per year, which is a bit less than in observations (e.g., $\sim$0.65 per year in the latest ERA-5 reanalysis). This may be due to the fact that in the climatology, the vortex is somewhat too strong and cold (see supplementary figure 1a) compared to in observations.

Every January 1st in CTRL, we generate a branched integration where a *transient* warming in the extratropical stratosphere is imposed in order to trigger a SSW. We refer to these runs with imposed warming perturbations as PTRB experiments herein. For each PTRB, there are 50 ensemble members (from the 50 years in CTRL). In order to impose a warming, the following zonally-symmetric term is added to the temperature tendency equation:

$$F(\varphi, p, t) = \tau(t)\Phi(\varphi)\Lambda(p), \tag{1}$$

where

$$\tau(t) = \begin{cases} 1, & \text{if } 0 < t - t_0 \leq N_\mathrm{d} \text{ days} \\ 0, & \text{otherwise,} \end{cases} \tag{2}$$

$$\Phi(\varphi) = -\frac{Q}{2}\left(1 - \tanh\left[\frac{\varphi - \varphi_0}{\Delta\varphi}\right]\right), \tag{3}$$

and

$$\Lambda(p) = \begin{cases} \frac{p - p_b}{p_t - p_b}, & \text{if } p_t < p < p_b \\ 1, & \text{if } p \leq p_t \\ 0, & p > p_b, \end{cases} \tag{4}$$

and where $t$ is the model time, $t_0$ is the reference time (midnight on December 31st), $N_d$ is the prescribed duration of the heating, $\varphi$, $\varphi_0$ and $\Delta\varphi$ are the latitude, reference latitude on which the warming starts and the width of the warming, $Q$ is the heating rate per day (units of K day$^{-1}$), and $p$ is the pressure level. The reference latitude and width are taken to be $\varphi_0$ =60°N and $\Delta\varphi$ =5°, respectively. To avoid sharp transitions in the vertical, the heating perturbation decreases linearly between $p_t$ and $p_b$ which we choose to be $p_t = 60$hPa and $p_b = 150$hPa so as to limit the heating to the stratosphere and to avoid minimal interference with the troposphere below. An example heating profile with $Q = 15$Kday$^{-1}$ is shown in figure 1a. Note that the stratospheric warming is applied to sigma levels rather than pressure levels, however the difference between the two is relatively small and hence does not affect our results quantitatively.

In total, 5 PTRB experiments are presented here, each with 50 ensemble members and with varying-magnitude warmings that are switched on for 3 days (i.e., $N_d = 3$ days); the maximum thermal forcing is $Q = 25\mathrm{Kday}^{-1}$, incrementally decreasing by 5K down to $Q = 5\mathrm{Kday}^{-1}$. For example, in the 15-K PTRB, a forcing of $Q = 15\mathrm{K\ day}^{-1}$ is switched on for 3 days, after which it is switched off and subsequently the model is allowed to run freely. Figure 1b shows the change in vortex strength (i.e., zonal-mean zonal wind $\overline{u}$ at 60°N and 10 hPa) for each of the five PTRB experiments (ensemble means shown in thick coloured lines) as well as the free-running CTRL (black line). By construction, the PTRB experiments follow CTRL throughout December until January 1st when the heating perturbation is switched on. The PTRB experiments then show a sudden weakening of the vortex followed by a slow recovery in the ensemble mean (although there is considerable spread among individual ensemble members as shown by the 15-K PTRB [thin grey lines]). The magnitude of the weakening of $\overline{u}$ increases with increasing thermal forcing, with the 5-K and 10-K PTRBs only weakening the vortex but with no reversal, whereas the 15-K, 20-K and 25-K PTRBs all show a reversal in the ensemble mean. Over the next 2-3 months, $\overline{u}$ recovers to a state that is close to that found in CTRL in March-April.

Note that PTRB experiments where the duration of the thermal forcing has lasted for longer than $N_d = 3$ days have also been conducted (e.g., for $N_d = 5$ and 10 days). However, the results are qualitatively similar to those presented in this paper. The key difference is that the initial disruption of the vortex persists for longer and there is hence a tropospheric impact which also lasts for longer in conjunction with the thermal forcing duration (this is particularly true in the

$N_d = 10$ days experiment). We focus on the $N_d = 3$-day experiments as the duration of the tropospheric impact compares favourably to that in CTRL.

The initial stratospheric and tropospheric states for each ensemble member are not the same and are essentially random. This is indicated by the spread of the individual ensemble members for the 15-K PTRB (thin grey lines) before January 1st in figure 1b. Hence, any signal in the PTRB-anomaly composites in relation to CTRL, represents the deterministic response to the thermally-forced stratospheric anomalies, which are thus, independent of the initial stratospheric and tropospheric states.

## 3. Results: Zonal-Mean Circulation and Wave Evolution During Free-Running and Thermally-Forced SSWs

We compare the evolution of the zonal-mean circulation and wave propagation/forcing between the 22 SSWs identified in CTRL (hereafter CTRL SSWs) and the thermally-forced SSWs in PTRB. We focus primarily on the 15-K PTRB experiment as the SSWs evolve most similarly to those in CTRL. Nevertheless, we also make inter-experiment comparisons to examine the tropospheric response sensitivity to the various-magnitude thermal forcings.

The anomalies in this section are all deviations away from the unfiltered daily climatology in CTRL. For example, the anomalies averaged over lags 1-3 in PTRB are calculated as the deviations away from the daily climatology in CTRL averaged over January 1st to 3rd.

### a. Zonal Wind, NAM and Temperature Evolution

Composites of zonal-mean zonal wind $\overline{u}$ (green contours) and zonal-mean temperature $\overline{T}$ (shading) are shown in figure 2 for different lag stages during the lifecycle of the CTRL SSWs (top row) and during the PTRB SSWs (bottom row). Prior to the onset (figure 2a), the CTRL SSWs are marked by both stratospheric and tropospheric precursors. In particular, there is a weaker and warmer polar vortex with largest magnitudes above $\sim$50 hPa. There is also evidence of tropospheric preconditioning with $\overline{u} < 0$ anomalies at high latitudes and $\overline{u} > 0$ south of $\sim$50°N. Such precursors have been evident in many other studies (e.g., Black and McDaniel 2004; Cohen and Jones 2011; Garfinkel et al. 2010). By construction, there are no anomalies in PTRB prior to the onset date (bottom).

Lags 1-3 (figure 2b) represent the early onset in CTRL SSWs and the forcing stage in PTRB SSWs. In CTRL, there is a clear intensification of the $\overline{u} < 0$ and $\overline{T} > 0$ anomalies in the stratosphere. In PTRB, the $\overline{T} > 0$ anomalies are located above 100 hPa by construction, and via thermal wind balance, give rise to a weakened polar vortex. Below $\sim$100 hPa, weak-valued $\overline{u} > 0$ anomalies centered on 60°N develop (although insignificant). These tropospheric $\overline{u}$ anomalies develop as a direct response to the heating perturbation aloft. In particular, in the region of heating, upwelling occurs, with corresponding downwelling at lower latitudes. To close the induced circulation, there is poleward motion below and equatorward motion aloft (not shown). The anomalous $\overline{u} > 0$ near 150 hPa, 60°N forms due to the Coriolis influence on the anomalous poleward motion.

As the lags progress, the development of the stratospheric anomalies in both CTRL and PTRB are rather similar. There is a poleward and downward movement of the $\overline{u}$ and $\overline{T}$ anomalies, with the $\overline{T}$ anomalies stalling in the lower stratosphere where they persist for up to three months (in agreement with the circulation development during polar-night jet oscillation events; Kuroda and Kodera 2001; Hitchcock et al. 2013). A recovery of the vortex starts in the upper stratosphere after 1-2 weeks due to the suppression of upward-propagating waves to higher levels (see later figures). In the troposphere, the $\overline{u}$ anomalies are somewhat different between CTRL and PTRB, with the former showing an intensification of the pre-existing tropospheric precursors and an equatorward shift by $\sim 5°$. In PTRB however, there is a downward propagation of the stratospheric $\overline{u} < 0$ anomalies into the troposphere, beginning at lags 11-20. In particular, the tropospheric $\overline{u} > 0$ anomalies found during the forcing stage (figure 2b) migrate equatorward and are replaced by high-latitude $\overline{u} < 0$ anomalies which occur as an extension of the negative $\overline{u}$ anomalies associated with the weakened polar vortex. Together, these anomalies yield a tropospheric dipole akin to that found during CTRL SSWs, although note that this dipole is initially located further poleward at lags up until lag $\sim$20.

To further highlight the downward propagation to the troposphere, figure 3 shows height-time composites of the Northern-Annular mode (NAM) index (shading) and $\overline{u}$ anomalies (contours) for the CTRL SSWs (a) and for the 25-K (b), 15-K (c) and 5-K (d) PTRB experiments. The NAM index is calculated as the area-averaged geopotential height anomalies north of 60°N, normalised by the standard deviation at each pressure level and multiplied by -1, as suggested by Baldwin and Thompson (2009), and $\overline{u}$ is averaged over 60-80°N. Prior to the onset, there are no anomalies by construction in all PTRB experiments, whereas the tropospheric precursors present in figure 2a are clearly present in CTRL (top). After the onset, the stratospheric anomalies are somewhat similar between CTRL and PTRB, with a sudden enhancement of negative NAM anomalies close to the onset date followed by recovery first aloft, and persistence in the lower stratosphere. The 25-K and 15-K PTRB appear to have largest-magnitude lower-stratospheric $\overline{u}$ anomalies at longer lags, although note that the NAM magnitude in the 5-K PTRB in May is similar to in the other two PTRB experiments.

In terms of the downward influence on the troposphere, the CTRL SSWs, 25-K and 15-K PTRB experiments exhibit the classical 'dripping-paint' pattern found by Baldwin and Dunkerton (2001). This is in contrast to the 5-K PTRB experiment which does not show any statistically-significant downward propagation below $\sim$200 hPa aside from a weakly-negative tropospheric NAM in March. In particular, in the 15-K and 25-K PTRB, the NAM and $\overline{u}$ anomalies gradually propagate down to $\sim$300-400 hPa over the first $\sim$15-20 days, which is then followed by a sudden, barotropic response down to the surface. Further, the 25-K PTRB shows evidence of the largest-magnitude and most persistent tropospheric response.

Note that the positive tropospheric NAM in the 25-K and 15-K PTRBs at early lags, represent the anomalous tropospheric westerlies found in figure 2 at lags close to the forcing. It is also worth noting that the second negative NAM peak in April-May in all PTRB experiments may be related to the final warming of the vortex, or may well be due to the systematic onset of a second SSW as the vortex recovers from the initial SSW event (where the recovery gives rise to favourable conditions for a second SSW). Such double-SSW type winters have been found in observations (e.g., Hitchcock et al. 2013), and also bear resemblance to periodic solutions found in simpler models (e.g., **?**).

In observations, the tropospheric $\overline{u}$ anomalies following a SSW event, project onto the leading mode of variability (i.e., the first empirical orthogonal function [EOF] of zonal wind) (e.g., Simpson et al. 2011) which represents latitudinal shifts in the near-surface zonal-mean tropospheric jet. To this end, we present $\overline{u}$ anomalies at 850 hPa for the CTRL SSWs as well as the projection of these anomalies onto the 1st and 2nd EOFs (hereafter referred to as EOF1 and EOF2 respectively) in figure 4a-c. Figure 4d-f shows the same except for the 15-K PTRB experiment. To calculate the EOFs, daily data for December-May is used, multiplied by $\sqrt{\cos\varphi}$ over 1-87N. It is clear that EOF1 represents latitudinal shifts in the climatological near-surface winds whereas EOF2 gives rise to a pulsing or broadening of the jet as expected (see green contours in panels d-f and horizontal line in a-c).

For the CTRL SSWs (left), a dipole in $\overline{u}$ exists with negative (positive) anomalies straddling the December-February climatological jet core (horizontal line) at both negative and positive lags. The dipole at negative lags again indicates the tropospheric precursors seen in previous figures, although the $\overline{u}$ anomalies have larger magnitudes after the onset. It is clear from figures 4b-c that the near-surface response to SSWs mostly projects onto EOF1, with a much smaller projection onto EOF2. However, we note that the projection onto EOF2 does become more pronounced after lag $\sim 30$ compared to at earlier lags.

For the 15-K PTRB experiment (right), the $\overline{u}$ anomalies project onto both EOF1 and EOF2. In agreement with figure 2, the $\overline{u} > 0$ anomalies initially start at higher latitudes before migrating equatorward and stalling at $\sim 45$N after about 20 days (and also becoming significant). The significant negative anomalies at higher latitudes, begin after $\sim 10$ days, in agreement with the $\sim 10$-day delay in thospheric response found in observations by Baldwin and Dunkerton (1999).

Looking more closely, the projection onto EOF2 precedes the projection onto EOF1 by $\sim 5-10$ days. This points to the equatorward shift of the anomalies as the lags progress. After $\sim 20$ days, $\overline{u}$ projects onto both EOFs, although with a bias towards EOF1 (compare magnitudes of e and f panels). This structure is somewhat reminscent of that during final warmings in agreement with Black et al. (2006) and Sheshadri et al. (2017) who found that the tropospheric response during final warmings is to project onto both EOF1 and EOF2. Nevertheless, we note the similarity between CTRL and PTRB at lags $\gtrsim 30$ where the projection onto EOF2 in CTRL becomes more pronounced.

A natural question arising from figures 2- 4 is how the strength of the initial stratospheric warming relates to the subsequent strength and persistence of the tropospheric response. Hence, in figure 5a, the variability of the strength of the tropospheric response for all ensemble members for all PTRB experiments is shown as a scatter plot of the lower-stratospheric (100-hPa) $\overline{u}$ averaged over lags 11-90, plotted against $\overline{u}$ at 850 hPa averaged over lags 11-90. Figure 5b then addresses how the persistence of the tropospheric NAM varies in response to the stratospheric anomalies as a scatter plot of the 100-hPa NAM averaged over lags 11-90, against the percentage of days post onset, that the NAM at 850 hPa is less than $-1$ standard deviation. Note that we use lag averages starting at lag 11 to limit the influence of the imposed forcing on the results. Nevertheless, the results are not sensitive to changes in the averaging lags, latitudes or pressure levels chosen, or to the NAM threshold used in (b).

Overall, it is clear that a more negative lower-stratospheric $\overline{u}$ anomaly and NAM index results in a more negative tropospheric $\overline{u}$ anomaly (a; strong positive correlation of $r = 0.87$) and persistent negative NAM (b; negative correlation of $r = -0.74$) closer to the surface. The ensemble mean for each PTRB experiment shows that a PTRB with stronger thermal forcing has a stronger and more persistent downward impact, although there is scatter amongst different experiments, particularly in (b). This is indicative of the fact that the vortex state prior to the thermal forcing being initialised was already highly variable with some runs having an anomalously weak or strong vortex. The regression slopes (top right) allow us to approximately quantify the magnitude of the downward impact. For instance, the near-surface $\overline{u}$ response to an SSW is $\sim$1/3 of the strength of the lower-stratospheric $\overline{u}$ anomaly averaged over positive lags. Further, an averaged lower-stratospheric negative NAM of one standard deviation, leads to $\sim 25-30\%$ of the following 90 days having a near-surface NAM of $< -1$ standard deviation. Note that if $\overline{u}$ anomalies at 10 hPa are used on the abscissa in (a), the correlation drops slightly to $r = 0.68$, athough this is still rather high compared to in previous studies (e.g., Maycock and Hitchcock 2015; White et al. 2019; Rao et al. 2019). If just the 22 CTRL SSWs are utilised in the calculation, then the correlations become $r$ =0.83 at 100 hPa and $r$ =0.43 at 10 hPa.

To further show that a stronger thermal perturbation yields a more-negative tropospheric NAM response, figure 5c shows histograms of the 850-hPa daily NAM indices at positive lags for the 25-K and 5-K PTRB experiments (only the means are shown for the other three intermediate experiments as coloured vertical lines, along with the ensemble mean for CTRL in grey). The main feature is that the 25-K PTRB leads to an overall shift of the tropospheric NAM towards more negative values in comparison to the 5-K PTRB rather than there being large changes in the skewness or kurtosis of the respective histograms (see values in top right). This is in agreement with Simpson et al. (2011), Sigmond et al. (2013) and Hitchcock and Simpson (2014) who also found that the main stratospheric influence is to bias the troposphere to a more negative NAM-like state. We note that the 15-K PTRB produces a near-surface response of very similar magnitude to in CTRL (compare pink and grey vertical lines).

In summary, the evolution of $\overline{u}$ and $\overline{T}$ in the CTRL SSWs and the thermally-triggered SSWs become very similar after $\sim$2-3 weeks. Prior to that, the thermally-triggered SSWs show a gradual poleward and downward migration of $\overline{u} < 0$ from the lower stratosphere to the near-surface at high latitudes, where they then migrate equatorward and stall at midlatitudes, projecting predominantly onto EOF1, and with a smaller projection onto EOF2. It appears that the strength of the tropospheric response to SSWs mostly depends on the magnitude of the heating perturbation in the lower stratosphere and acts to bias the tropospheric NAM to a more negative state.

Herein, the lag stages 4-10 and 11-20 are averaged into one (4-20). This is because the aim of this paper is to examine the long-lag (i.e., $\gtrsim$3-week) tropospheric response to SSWs. The mechanisms behind the initial downward impact (i.e., the short-lag response), are beyond the scope of this paper.

### *b. Planetary- and Synoptic-Wave Evolution*

In this section we examine the wave evolution during SSWs in both the CTRL and PTRB experiments. In particular, we plot the Eliassen-Palm (EP) flux $\mathbf{F} = (F^{(\varphi)}, F^{(z)})$, where

$$F^{(\varphi)} = a\rho_0 \cos\varphi \left( \overline{u}_z \frac{\overline{v'\theta'}}{\overline{\theta}_z} - \overline{u'v'} \right) \tag{5a}$$

$$F^{(z)} = a\rho_0 \cos\varphi \left[ \left( f - \frac{(\overline{u}\cos\varphi)_\varphi}{a\cos\varphi} \right) \frac{\overline{v'\theta'}}{\overline{\theta}_z} \right] \tag{5b}$$

are the meridional and vertical components of the EP flux in spherical coordinates. In these equations, $z$ is the log-pressure height, $v$ and $w$ are the meridional and vertical components of the wind, $\theta$ is the potential temperature, and $a$, $f$ and $\rho_0$ are the Earth's radius, Coriolis parameter and background density profile. Overbars and primes represent zonal averages and the deviations therefrom, respectively. The divergence of $\mathbf{F}$:

$$\Pi \equiv \frac{\nabla \cdot \mathbf{F}}{\rho_0 a \cos\varphi} \tag{6}$$

$$= \frac{1}{\rho_0 a \cos\varphi} \left( \frac{1}{a\cos\varphi} \frac{\partial}{\partial \varphi} (F^{(\varphi)} \cos\varphi) + \frac{\partial F^{(z)}}{\partial z} \right) \tag{7}$$

in the zonal-mean zonal momentum budget:

$$\frac{\partial \overline{u}}{\partial t} + \overline{v}^* \left[ \frac{(\overline{u}\cos\varphi)_\varphi}{a\cos\varphi} - f \right] + \overline{w}^* \frac{\partial \overline{u}}{\partial z} = \frac{\nabla \cdot \mathbf{F}}{\rho_0 a \cos\varphi} + \overline{X} \tag{8}$$

represents the wave forcing of $\overline{u}$ (Andrews et al. 1987), and ($\overline{v}^*$, $\overline{w}^*$) and $\overline{X}$ represent the meridional and vertical components of the residual mean meridional circulation (see section 3 d) and nonconservative effects/parameterised gravity-wave drag, respectively. Hence, a convergence of wave activity ($\nabla \cdot \mathbf{F} < 0$) acts to weaken $\overline{u}$ and and vice versa, although on longer timescales, the main balance in eq. 8 is between $\Pi$ and the $\overline{v}^*$ term in brackets. In particular, $\nabla \cdot \mathbf{F} < 0$ is balanced by a poleward residual circulation $f\overline{v}^* > 0$, and vice versa (e.g., Martineau et al. 2018). The wavenumber contributions to $\mathbf{F}$ and $\Pi$ can be quantified by first filtering $u$, $v$, $w$ and $\theta$ using a Fourier transform. Note that in this section, and in all subsequent figures which involve eddy contributions, the lowest level of the plots are cut-off at 700 hPa. This is to avoid issues with topography when decomposing variables into different wavenumbers.

Figure 6 shows latitude-height composites of the EP flux divergence term $\Pi = \nabla \cdot \mathbf{F}/\rho_0 a \cos\varphi$ (shading), EP fluxes $\mathbf{F}$ (arrows) and $\overline{u}$ (contours; as in figure 2) anomalies for the CTRL SSWs at various lag stages (note that lags 4-10 and 11-20 in figure 2 have been averaged together here in c). $\mathbf{F}$ is split into planetary wave (zonal wavenumbers 1-3; top) and synoptic wave (wavenumbers 4+; bottom) contributions. Note that $\mathbf{F}$ is plotted only if $F^{(\varphi)}$ or $F^{(z)}$ is significantly different from the climatology. Prior to lag zero (a), the weaker vortex is driven by an enhanced convergence of upward-propagating planetary-wave anomalies throughout the high-latitude stratosphere (dominated by wave 1). There is also convergence in the troposphere north of 45°N which appears to contribute to the precursory equatorward jet shift. At lags 1-3 (b), there is continued convergence of planetary waves inside the polar vortex as well as at 45°N in the mid- to lower troposphere, along with anomalous $\Pi > 0$ in the high-latitude upper troposphere. The planetary-wave anomalies mostly enter the stratosphere at ~40-50°N rather than at higher latitudes, which is likely a response to the weaker vortex. In the midlatitude stratosphere, the anomalous synoptic-wave convergence may result from breaking planetary waves which generate smaller-scale features.

At lags 4+ (c-d) planetary-wave $\mathbf{F}$ anomalies are generally oriented poleward and downward along with anomalous $\Pi > 0$ in the high-latitude stratosphere, although the magnitudes of $\mathbf{F}$ and $\Pi$ for planetary waves decreases at lags 21-90. This suppression following a SSW is the expected response to the weakened polar vortex (e.g., Limpasuvan et al. 2004). The presence of tropospheric precursors makes it difficult to separate the anomalies which are associated with the downward propagation from the preexisting tropospheric anomalies. The region of anomalous planetary-wave $\Pi < 0$ near 55-60°N in the middle troposphere contributes to the maintenance of the negative high-latitude $\overline{u}$ anomalies.

Tropospheric poleward-propagating synoptic waves are present at all lags straddling the $\overline{u}$ dipole. In particular, they likely are very important in maintaining the persistent tropospheric jet shift via equatorward momentum fluxes (e.g., Limpasuvan et al. 2004).

We now compare the anomalies in the CTRL SSWs with those for the 15-K PTRB in figure 7, which shows the same as figure 6 except without panels at negative lags. At lags 1-3 (a), a vertical dipole in $\Pi$ for planetary waves is evident which straddles the lowest level of maximum forcing at $\sim$60 hPa, with anomalous divergence aloft, and convergence extending down to $\sim$200 hPa. This dipole is associated with anomalous downward-propagating planetary waves and occurs as a direct response to the weakened vortex. In particular, the weakening vortex lowers the critical lines and hence prevents Rossby waves from propagating freely. The increase in static stability associated with the thermal forcing may also play a role in reducing the upward propagation of planetary waves (see eq. (5)b and Chen and Robinson 1992). This will also be explained by refractive-index arguments in section 3 c. In the region of anomalous tropospheric $\overline{u} > 0$, there is anomalous weak-valued synoptic waves which propagate upward and converge in the lower stratosphere, consistent with the larger propagation window for smaller-scale waves (see Charney and Drazin 1961).

At lags 4-20 (i.e., after the forcing has been switched off; b), the planetary-wave anomalies are more widespread with an anomalous poleward and downward propagation extending from the stratospheric subtropics down to the high-latitude troposphere and with divergence aloft and convergence in the lower-stratosphere-upper-troposphere. In particular, the $\mathbf{F}$ anomalies extend down to 700 hPa in conjunction with the $\overline{u} < 0$ anomalies at high latitudes. In terms of synoptic waves, a fountain of anomalies is apparent at midlatitudes with convergence in the stratosphere. These anomalous synoptic waves may originate due to the enhanced baroclinicity associated with the anomalous tropospheric westerlies but are also consistent with the enhanced ability to propagate into the stratosphere as the vortex weakens.

At lags 21-90 (c), both the planetary-wave and synoptic-wave anomalies are similar to those in CTRL (figure 6). The planetary-wave anomalies are essentially the same as at earlier lags, but with weaker magnitude as the vortex recovers. In terms of synoptic waves, there are clear poleward-propagating anomalies straddling the tropospheric $\overline{u}$ dipole, necessary to maintain the $\overline{u}$ anomalies against surface friction.

We next investigate the source of the tropospheric poleward-propagating synoptic waves. In figure 8a, a latitudinal profile of the Eady growth rate ($\sigma = 0.31|f||\partial u(\varphi,z,t)/\partial z|/N$) anomalies (Hoskins and Valdes 1990, blue line) at 400 hPa, averaged over lags 21-90 is shown for the 15-K PTRB. Also shown are the corresponding 400-hPa $\overline{u}$ (black line) and synoptic-wave $F^{(z)}$ (red line) anomalies. Note that similar results are obtained at other tropospheric levels. At midlatitudes (high latitudes), the dipole of $\overline{u} > 0$ ($\overline{u} < 0$) anomalies is collocated with $F^{(z)} > 0$ ($F^{(z)} < 0$) and $\sigma > 0$ ($\sigma < 0$). This suggests that in the midlatitude region of enhanced baroclinicity, there is an enhanced generation of synoptic waves, in contrast to at higher latitudes, where generation is reduced. Although it is difficult to establish conclusively from the EP fluxes and Eady growth rate alone, these upward-propagating synoptic waves propagate poleward and drive the persistent jet shift (figure 7) in a positive feedback as suggested by Robinson (2000). The midlatitude region of $\sigma > 0$ is located further poleward at earlier lags and migrates equatorward alongside the $\overline{u}$ anomalies (not shown).

To determine if the poleward-propagating synoptic waves in figure 7 are reflected, or break closer to the Pole, the total wavenumber

$$K^* = \cos\varphi \left( \frac{\beta^*}{\overline{u} - c} \right) \tag{9}$$

(Hoskins and Karoly 1981) as a function of latitude at 500 hPa is plotted in figure 8b for all PTRB experiments averaged over lags 21-90 (we assume $c = 0$[1]). In eq. 9, $\beta^*$ is the absolute vorticity in spherical coordinates. This diagnostic shows that a Rossby wave will be turned at a latitude where $k = K^*$ (i.e., where the meridional wavenumber becomes zero), will propagate towards regions of larger $K^*$, before breaking at a critical latitude at which $\overline{u} = c$ and $K^*$ becomes infinite. South of $\sim 55°$N, the DJF-climatological $K^*$ in CTRL (grey line) and PTRB $K*$ (coloured lines) are essentially inseparable. However, in the region of easterly $\overline{u}$ anomalies further poleward, the PTRB experiments diverge from the CTRL with a $K^*$ peak at $\sim 65°$N. For stronger thermal forcing, this peak in $K^*$ becomes more prominent towards higher wavenumbers. In the region of the $K^*$ peak, linear theory suggests that meridionally-propagating synoptic waves are essentially trapped due to the presence of turning latitudes on both the poleward and equatorward flanks (evidenced by $K^* \to 0$) and will eventually break. Note that the peak becomes more pronounced and extends to higher zonal wavenumbers at lower levels (not shown). The increase in $K^*$ for stronger PTRB experiments indicates that a stronger stratospheric warming, leads to a stronger synoptic-wave response.

To understand if the magnitude of the thermal forcing influences the strength of the tropospheric synoptic-wave anomalies, figure 8c shows a scatter graph of the 100-hPa high-latitude $\overline{u}$ averaged over lags 11-60 plotted against the synoptic-wave $F^{(\varphi)}$ at 400 hPa and averaged over 45-55N and lags 11-60. Note that the results in the scatter plot are not sensitive to variations in the averaging lags or latitudes. Overall, the correlation coefficient between the two is $r$ =-0.68, indicating a fairly-strong relationship; i.e., a warmer stratospheric temperature perturbation gives rise to

[1]Note that upon including $c > 0$, the $K^*$ peak is evident at sub-polar latitudes (see below), but north of $\sim 60°$N, $K^*$ becomes imaginary (and hence represents wave evanescence). To better highlight the peak at sub-polar latitudes therefore, we use a value of $c = 0$.

a stronger tropospheric eddy momentum flux response. Nevertheless, despite the fact that the ensemble means for each of our PTRB experiments (represented by the coloured squares) show a near linear relationship, there is much variability around the individual ensemble members (coloured diamonds).

Overall, it appears that poleward-propagating synoptic waves play a key role in the maintenance of the equatorward-shifted tropospheric jet at longer lags in both the CTRL and PTRB SSWs. Such waves appear to be generated by the enhanced baroclinicity at midlatitudes, and propagate poleward where they break in the region of easterly anomalies (although note that such breaking was diagnosed using $K^*$ and not the EP flux convergence). planetary waves on the other hand, are suppressed throughout the stratosphere and troposphere and may play a key role at short lags in initially bringing the polar-vortex anomalies to the troposphere; however, examination of the initial downward communication is left to a future study.

### *c. Waveguide Evolution*

In order to determine if the changes in wave propagation shown in section 3b are consistent with that expected due to wave refraction in response to the evolving zonal-mean basic state, we now examine the refractive index:

$$n^2 = \frac{1}{\overline{u}-c}\overbrace{\left[2\Omega\cos\varphi - \left(\frac{(\overline{u}\cos\varphi)_\varphi}{a\cos\varphi}\right)_\varphi - \frac{a}{\rho_0}\left(\frac{\rho_0 f^2}{N^2}\overline{u}_z\right)_z\right]}^{\equiv\overline{q}_\varphi} \tag{10}$$

$$-\frac{k^2}{a^2\cos^2\varphi} - \frac{f^2}{4N^2H^2} \tag{11}$$

(e.g., Matsuno 1970) where $\overline{q}_\varphi$ is the meridional gradient of quasi-geostrophic potential vorticity (PV), $N^2$ is the static stability, $k$ is the zonal wavenumber, $c$ is the phase speed, $H$ is the density-scale height, and all remaining variables are as in earlier equations. Even though strictly speaking, the refractive index is valid only under the assumption of a slowly-varying basic state (i.e., the Wentzel-Kramers-Brillouin [WKB] theory for linear wave propagation), which is clearly not the case here, many previous studies have shown that the refractive index can provide useful information despite the fact that their experiments may not satisfy the underlying assumptions (e.g., Chen and Robinson 1992; Simpson et al. 2009; Garfinkel et al. 2012). It is expected in this framework, that waves tend to preferentially propagate away from regions of small $n^2$ towards regions of larger $n^2$. Waves cannot propagate in regions of $n^2 < 0$. Close to a critical line (where $\overline{u} = c$), $n^2$ becomes extremely large.

To calculate $n^2$ for the CTRL SSWs, we first average $\overline{u}(\varphi, z, t)$ and $N^2$ over the required lag stages and over all SSWs. $N^2$ is then further averaged vertically in the stratosphere (after pressure weighting), although using an $N^2$ profile which varies with height does not change the results qualitatively. The $n^2$ and $\overline{q}_\varphi$ anomalies for CTRL shown in figure 9 (top) are then calculated by subtracting the December-February climatology of $n^2$ and $\overline{q}_\varphi$. Note that in difference plots such as those presented here, the latter two terms in eq. (10) cancel out and hence the anomalies are the same for all wavenumbers. Note that $c = 0$ is used in eq. (10). The calculation of $n^2$ and $\overline{q}_\varphi$ for the PTRB experiments are calculated similarly except that $N^2$ is averaged over December to May (i.e., the length of each PTRB ensemble member) and over all ensemble members, and the anomalies are calculated as deviations from the corresponding lags in the CTRL daily climatology.

Figure 9 shows composites of $n^2$ and $\overline{q}_\varphi$ anomalies averaged over the same lags as in figure 2 for the CTRL SSWs (top) and for the 15-K PTRB (bottom). Note that the full field for both CTRL and PTRB is provided in figure 2 in the supplementary material. Focusing first on the CTRL SSWs (top), one of the most noticeable features is the high-latitude tropospheric region of anomalous $n^2 > 0$, associated with the tropospheric $\overline{u}$ anomalies (figure 2). This $n^2 > 0$ feature would be expected to encourage wave propagation towards it, as indeed seen in figure 6 with anomalous planetary-wave $F^{(z)} < 0$ and anomalous tropospheric synoptic-wave $F^{(\varphi)} > 0$. Aloft, the weakening vortex is indicated by negative $\overline{q}_\varphi$ anomalies. Note that there does not appear to be any preferential cavity for enhanced upward wave propagation prior to the onset, in the sense of focusing planetary waves onto the Pole.

A developing feature at positive lags is a region of $n^2 < 0$ in the midlatitude-subpolar upper-troposphere-lower-stratosphere which intensifies as the lags progress. Upon comparison with the December-February climatology of $n^2$ (see supplementary figure 1b), it appears that this feature extends the subtropical-midlatitude minimum of $n^2$ to higher latitudes, and hence, may act to shield the stratosphere from subsequent upward wave propagation. Nevertheless, we note that tunneling of planetary waves through a region of $n^2 < 0$ is still possible (e.g., Harnik 2002). Above $\sim$ 50 hPa, $n^2$ becomes positive after lags 1-3, as the vortex starts to recover (i.e., $\overline{u}$ returns to positive).

We now examine the PTRB SSWs (bottom). During the forcing stage (b; lags 1-3), the $n^2$ anomalies exhibit a vertical tripole in the extratropics, with an $n^2 > 0$ anomaly in the upper troposphere to lower stratosphere, and $n^2 < 0$ both above and below. This vertical tripole is the perhaps expected response given the high-latitude thermal forcing. Note that the region of anomalous high-latitude tropospheric $n^2 < 0$ occurs due to the anomalous tropospheric westerlies (see figure 2b). The negative (positive) PV gradient in the middle-upper (lower) stratosphere is also the expected response given the forcing. These $n^2$ anomalies agree dynamically with the $\mathbf{F}$ anomalies in the top row of figure 7, whereby there is convergence in the region of $n^2 > 0$ and divergence above and below.

At lags 4+ (c-d), $n^2$ and and $\overline{q}_\varphi$ become rather similar to in CTRL. In particular, the region of $n^2 < 0$ in the middle-to-lower stratosphere develops and becomes larger in magnitude as the lags progress. In the high-latitude troposphere, the region of anomalous $n^2 < 0$ at lags 1-3, completely switches sign to $n^2 > 0$. This region of $n^2 > 0$ becomes larger in magnitude as the lags progress, occurring in response to the $\overline{u} < 0$ anomalies associated with the weaker vortex aloft which have started their descent to the troposphere, and due to the fact that the tropospheric $\overline{u} > 0$ anomalies have shifted more equatorward. As aforementioned, these two features act to shelter the stratosphere from further upward planetary-wave propagation and to encourage enhanced poleward wave propagation (figure 7). The poleward-propagating synoptic waves may indeed play a role in the intensification of this feature, via a positive feedback: poleward synoptic waves flux momentum equatorward which intensifies the easterly anomalies at high latitudes, and thus intensifies the ambient refractive index (the high-latitude westerlies do not actually reverse). Consequently, this encourages further poleward synoptic-wave propagation.

Overall, as was the case in sections 3a-b, after ~3 weeks, the $n^2$ anomalies in the thermally-forced SSWs become similar to those in the CTRL SSWs. In particular, the mid-to-high-latitude lower-tropospheric $n^2 > 0$, the midlatitude lower-stratospheric $n^2 < 0$, and the large positive $n^2$ above $\sim$ 50 hPa, are all common features to CTRL and PTRB. The EP fluxes in section 3b agree dynamically with the $n^2$ anomalies here, and in particular, the high-latitude tropospheric region of $n^2 > 0$ first develops in response to the downward migration of the stratospheric $\overline{u}$ from aloft, before intensifying in an apparent positive feedback with the (likely) baroclinically-induced poleward-propagating synoptic waves.

*d. Meridional Circulation Evolution*

Wave activity propagation and forcing is intimately linked to the meridional circulation. To examine the evolution of the meridional circulation during SSWs in relation to the wave-forcing anomalies in the previous section, we examine the residual meridional mass streamfunction:

$$\begin{aligned}\Psi^* = \int_z^\infty \rho_0 \overline{v}^* \cos\varphi dz &= \int_z^\infty \rho_0 \left[\overline{v} - \frac{1}{\rho_0}\frac{\partial}{\partial z}\frac{\rho_0 \overline{v'\theta'}}{\overline{\theta}_z}\right]\cos\varphi dz \\ &= \int_z^\infty \rho_0 \overline{v}\cos\varphi dz + \frac{\rho_0\overline{v'\theta'}}{\overline{\theta}_z}\cos\varphi \equiv \Psi_{\overline{v}} + \Psi_{\overline{v'\theta'}}\end{aligned}$$

which approximates the Lagrangian-mean circulation of air parcels (e.g., Andrews et al. 1987, and see eq. 8). $\Psi_{\overline{v}}$ and $\Psi_{\overline{v'\theta'}}$ represent the Eulerian-mean meridional circulation and eddy heat flux contributions to $\Psi^*$, respectively. We present the evolution of $\Psi^*$ during SSWs.

Figure 10 shows composites of $\Psi^*$ (top) at various lag stages for the CTRL SSWs. At negative lags (a), $\Psi^*$ is everywhere positive aside from a small insignificant region in the troposphere at $\sim$30°N as well as in the tropics. This is indicative of a strengthened Brewer-Dobson circulation during the lead-up to a SSW. This is driven by an imbalance between the enhanced upward-propagating planetary-wave activity ($\Psi_{\overline{v'\theta'}} > 0$) and the induced thermally-indirect equatorward Eulerian-mean circulation ($\Psi_{\overline{v}} < 0$; not shown). The latter, upon being influenced by the Coriolis force, yield the easterly $\overline{u}$ anomalies associated with the weakened polar vortex (Matsuno 1971). At lags 1-3, the stratosphere still has a strengthened Brewer-Dobson circulation, although at lags 4+, these positive anomalies become weakly negative, due to the cutoff of planetary waves (see figure 6).

The tropospheric $\Psi^*$ response at positive lags is an extratropical tripole with $\Psi^* > 0$ at midlatitudes flanked at low and high latitudes by $\Psi^* < 0$ (although the high-latitude cell is much weaker at lags 4+). This tripole corresponds to changes in the width of the Polar, Ferrel and Hadley cells (e.g., Martineau et al. 2018). Indeed, this tripole is the response associated with general stratospheric NAM variability rather than variability solely attributed to the tropospheric NAM (see supplementary figure 3). We note that $\Psi^* < 0$ ($\Psi^* > 0$) at $\sim$30-45N ($\sim$45-65N) which straddles the nodal line in $\overline{u}$, is the meridional circulation response to the synoptic-wave $F^{(\varphi)} > 0$ (i.e., $\overline{u'v'} < 0$) anomalies (figure 6). In particular, the latitudinal gradients in $F^{(\varphi)}$ (i.e., the horizontal eddy forcing) straddling the nodal line, act to drive the zonal-mean state away from thermal wind balance, which necessitates the development of a pair of anomalous meridional circulation cells as shown in figure 10 (see eqs. 6- 8). This is the same as that explained in Haigh et al. (2005) using the Eulerian-mean momentum budget. The $\Psi^* < 0$ anomalies further poleward (i.e., the polar branch of the tripole) occur as a result of an imbalance between the $\Psi_{\overline{v'\theta'}}$ and associated $\Psi_{\overline{v}}$ anomalies (not shown).

The bottom row of figure 10 shows $\Psi^*$ anomalies for the 15-K PTRB experiment. Note that $\Psi^*$ is qualitatively similar for all of our experiments. At lags 1-3 (i.e., during the forcing stage; a), $\Psi^*$ is everywhere negative, with largest magnitudes at $\sim$55N, $\sim$50 hPa, and a second peak at $\sim$ 45N, 500 hPa. The $\Psi_{\overline{v}}$ contribution dominates $\Psi^*$ with $\Psi_{\overline{v}} < 0$ everywhere (not shown); this is the expected response and is similiar to the instantaneous response to a diabatic heating anomaly found in Shepherd et al. (1996) (their figure 2a), although their heating was centered at midlatitudes and hence had a weaker secondary circulation cell at higher latitudes. In particular, the imposed diabatic heating anomaly is balanced by rising motion over the Pole, and descending motion further equatorward, which by mass continuity gives rise to poleward (equatorward) motion in the upper troposphere (upper stratosphere). The contribution of $\Psi_{\overline{v'\theta'}}$ is that of a dipole straddling the lowest level of forcing (lower horizontal line; as in figure 7).

At lags 4-20 (c), the $\Psi^*$ anomalies are noticeably different to those in CTRL. For instance, the anomalous meridional circulation between $\sim$400 hPa and $\sim$ 50 hPa completely reverses to $\Psi^* > 0$. This occurs due to a slight imbalance between $\Psi_{\overline{v}} > 0$ and $\Psi_{\overline{v'\theta'}} < 0$ (not shown). Below 400 hPa, there are insignificant $\Psi^* < 0$ anomalies.

However, by lags 21-90, the $\Psi^*$ anomalies appear to be very similar to those in CTRL, with an extratropical tripole in the troposphere and with weakly-negative stratospheric anomalies. The tripole is the response to general stratospheric NAM variability and gives rise to changes in the width of the Ferrel cell, whereas the weakly-negative $\Psi^*$ aloft is the response to the reduced upward-propagating planetary waves into the stratosphere (figure 7). Hence, after $\sim$3 weeks, the circulation following the CTRL SSWs and that following the thermally-forced SSWs in PTRB become very similar to one another.

In summary, there are large differences in $\Psi^*$ between the CTRL SSWs and the thermally-forced SSWs at lags of less than $\sim$3 weeks. However, at longer lags, the $\Psi^*$ anomalies evolve very similarly with a tropospheric tripole associated with the shifted jet, and a weakly-negative stratospheric $\Psi^*$ associated with the suppressed planetary waves following the SSW onset (see section 3b).

## 4. Summary and Discussion

We have examined the tropospheric response to varying-magnitude high-latitude stratospheric heating perturbations in order to examine the downward influence of SSWs. To capture the sudden nature of a SSW, the heating perturbation was only switched on for a few days (spun-off from a free-running control integration, CTRL), which, depending on the magnitude of the imposed heating, either gave rise to a weakened, or completely reversed vortex. The evolution of the thermally-forced SSWs was then compared with naturally-occurring SSWs identified in CTRL. Our novel approach has allowed us to isolate the tropospheric response associated with the weakened polar vortex, as opposed to the response associated with the original planetary waves (and hence momentum torques) which initiated the SSW. We have focussed in particular on understanding the long-lag (i.e., >2-3 weeks) tropospheric response as opposed to the initial comminication of the stratospheric anomalies to the troposphere at shorter lags.

Our results confirm a downward influence from the stratosphere following a SSW event (e.g., Baldwin and Dunkerton 2001). This is evidenced by the strong tropospheric signal following the thermally-forced SSWs (figures 2- 5) despite the fact that there are no momentum torques associated with preceding planetary waves which initiate the SSW (as is the case in the free-running CTRL SSWs). Plumb and Semeniuk (2003) demonstrated that the tropospheric zonal-wind anomalies following a SSW could occur passively in response to the upward-propagating planetary waves which initiated the SSW, and hence concluded that a downward migration of wind anomalies is not necessarily indicative of a downward stratospheric influence. Our results unambiguously confirm that a weakening of the stratospheric polar vortex drives a tropospheric circulation response.

Another key result is that at longer lags, the stratospheric and tropospheric evolution in the free-running CTRL SSWs and the thermally-forced SSWs are remarkably similar, both in terms of the zonal-mean circulation and the eddy fluxes (figures 2, 6- 7, 9, 10). This indicates that at longer lags the tropospheric response is somewhat generic and the initial formation of a SSW does not play a large role. Instead, the strength of the warming in the lower stratosphere, determines the magnitude of the tropospheric response (figure 5, and in agreement with, e.g., Maycock and Hitchcock 2015). Nevertheless, at shorter lags, the particulars associated with the initial SSW formation may play a potentially important role, given the difference in evolution between the CTRL SSWs and PTRB SSWs.

In maintaining the tropospheric jet shift at longer lags, synoptic waves play a key role (see figures 6- 8), in agreement with a number of studies (e.g., Limpasuvan et al. 2004; Polvani and Waugh 2004; Song and Robinson 2004; Domeisen et al. 2013). The collocation of upward-propagating synoptic waves and the peak Eady growth rate in the region of midlatitude westerly anomalies suggests that synoptic waves may be forced due to the enhanced baroclinicity (see figure 8 and e.g., Robinson 2000). The poleward-propagation of these synoptic waves then appear to generate a positive feedback in concert with the region of enhanced high-latitude tropospheric refractive index that develops in response to the descending polar-vortex anomalies, and intensifies as the lags progress (figure 9). In particular, the poleward-propagating synoptic waves flux momentum equatorward (see eq. 5a) and thus weaken the winds further at high latitudes, which in turn enhances the ambient refractive index (due to $\overline{u}-c$ in the denominator of eq. 10) and subsequently encourages more poleward synoptic-wave propagation. This explanation is similar to that in Simpson et al. (2009) who suggest a change in the refractive index to initiate changes in momentum fluxes which feedback on the ambient refractive index. We note that the poleward-propagating synoptic waves and $n^2$ feature were also present at all lags in CTRL; at negative lags it was associated with the tropospheric precursors. However, whether this feedback mechanism plays a role during observed SSWs requires further work.

The initial 3-week period after January 1st in the PTRB experiments during which the polar-vortex anomalies migrate downward to the surface, requires further investigation. The circulation anomalies gradually propagate down to $\sim$ 300 hPa over the first $\sim$ 2 weeks, before they barotropically extend downward to the high-latitude lower troposphere (figure 3). The suppression of planetary waves appears to correlate with this downward propagation (figure 7) in agreement with Hitchcock and Haynes (2016) and Hitchcock and Simpson (2016). Once the mean-state anomalies reach the lower troposphere, they subsequently migrate equatorward before stalling at midlatitudes where they straddle the midlatitdue jet (figures 2 and 4). The exact mechanisms for this downward and subsequently equatorward migration of the winds is beyond the scope of this paper.

Unlike in our CTRL run (as well as in observations), for which the near-surface response following a SSW projects almost entirely onto the first EOF, the near-surface response following the PTRB SSWs projects onto both the first and second EOFs (figure 4), although with a larger projection onto EOF1. Some parallels can therefore be drawn between the PTRB SSWs and the observed response during final warmings (which, for our stronger experiments, is particularly true as the vortex completely reverses; figure 1b). In particular, Black et al. (2006) and Sheshadri et al. (2017) found that the tropospheric response following a final warming, is a projection onto both of the first two EOFs. The latter study suggested that often the response following such stratospheric variability is to project onto both EOFs, and that the two cannot be seen as independent. In fact, the projection onto EOF2 leads the projection onto EOF1 by $\sim 5-10$ days, indicative of the equatorward migration of the $\overline{u}$ anomalies from high to mid latitudes where they stall (figure 2). Hence, our experiments may be useful for examining the tropospheric response to a wide-range of polar-vortex variability, although in this study, we have focussed on SSWs.

It should be noted that the mechanisms for downward propagation discussed here are based on the evolution during thermally-triggered SSWs, which, by construction, lack the vital ingredient of planetary-scale momentum torques that are ultimately responsible for observed SSWs. The meridional circulation anomalies associated with heating and momentum torques can be very different (e.g., Shepherd et al. 1996) and hence could conceivably have different effects on the troposphere. Nevertheless, given the similar evolution of the thermally-forced SSWs to the CTRL SSWs at longer lags, these initial momentum torques seemingly do not play a large role in the tropospheric response at subseasonal to seasonal timescales.

It has been suggested that the strength of the original wave driving can be important for the tropospheric response to some SSWs (e.g., Nakagawa and Yamazaki 2006; White et al. 2019). This is somewhat similar to the strength of the lower-stratospheric warming in our study. It has also been suggested that the troposphere may need to be in a state to 'receive' the stratospheric influence (e.g., Black and McDaniel 2004). We agree that the details of an SSW are important for the evolution of a SSW, as well as for the intiial downward impact on the troposphere, but argue that the long-lag response of the tropospheric jet is a generic response to a weakened polar vortex.

*Acknowledgments.* We thank Hua Lu for useful discussion. We acknowledge the support of a European Research Council starting grant under the European Union Horizon 2020 research and innovation programme (Grant Agreement 677756). EPG also acknowledges support from the U.S. NSF through Grant AGS-1852727. MJ is supported by the ARC Centre of Excellence for Climate Extremes under Grant CE170100023 and ARC grant FL150100035. JR also acknowledges support from the National Natural Science Foundation of China (41705024).

## References

Alexander, M., and T. J. Dunkerton, 1999: A spectral parameterization of mean-flow forcing due to breaking gravity waves. *J. Atmos. Sci.*, **56**, 4167–4182.

Ambaum, M. H. P., and B. J. Hoskins, 2002: The NAO troposphere-stratosphere connection. *J. Atmos. Sci.*, **15**, 1969–1978.

Andrews, D. G., J. R. Holton, and C. B. Leovy, 1987: *Middle Atmosphere Dynamics*. Academic Press, 489 pp.

Baldwin, M. P., and T. J. Dunkerton, 1999: Propagation of the Arctic Oscillation from the stratosphere to the troposphere. *J. Geophys. Res.*, **104**, 30 937–30 946.

Baldwin, M. P., and T. J. Dunkerton, 2001: Stratospheric harbingers of anomalous weather regimes. *Science*, **294**, 581–584.

Baldwin, M. P., and D. W. J. Thompson, 2009: A critical comparison of stratosphere-troposphere coupling indices. *Q. J. R. Meteorol. Soc.*, **135**, 1661–1672.

Betts, A., 1986: A new convective adjustment scheme. part II: Observational and theoretical basis. *Q. J. R. Meteorol. Soc.*, **112**, 677–691.

Betts, A., and M. Miller, 1986: A new convective adjustment scheme. part II: Single column tests using gate waves, BOMEX, ATEX and arctic air-mass datasets. *Q. J. R. Meteorol. Soc.*, **112**, 693–710.

Black, R. X., and B. A. McDaniel, 2004: Diagnostic case studies of the northern annular mode. *J. Clim.*, **17**, 3990–4004.

Black, R. X., B. A. McDaniel, and W. A. Robinson, 2006: Stratosphere-troposphere coupling during spring onset. *J. Clim.*, **19**, 4891–4901.

Charlton, A. J., and L. M. Polvani, 2007: A new look at stratospheric sudden warmings. Part I: Climatology and modeling benchmarks. *J. Clim.*, **20**, 449–469.

Charney, J. G., and P. G. Drazin, 1961: Propagation of planetary scale disturbances from the lower into the upper atmopshere. *J. Geophys. Res.*, **66 (1)**, 83–109.

Chen, P., and W. A. Robinson, 1992: Propagation of planetary waves between the troposphere and stratosphere. *J. Atmos. Sci.*, **49 (24)**, 2533–2545.

Cohen, J., and J. Jones, 2011: Tropospheric precursors and stratospheric warmings. *J. Clim.*, **24**, 6562–6572.

Cohen, N. Y., E. P. Gerber, and O. Buhler, 2014: What drives the Brewer-Dobson circulation? *J. Atmos. Sci.*, **71**, 3837–3855.

Domeisen, D. I. V., L. Sun, and G. Chen, 2013: The role of synoptic eddies in the tropospheric response to stratospheric variability. *Geophys. Res. Lett.*, **40**, 4933–4937.

Frierson, D. M., I. M. Held, and P. Zurita-Gotor, 2006: A gray-radiation aquaplanet moist gcm. part I: Static stability and eddy scale. *J. Atmos. Sci.*, **63**, 2548–2566.

Garfinkel, C. I., D. L. Hartmann, and F. Sassi, 2010: Tropospheric precursors of anomalous northern hemisphere stratospheric polar vortices. *J. Clim.*, **23**, 3282–3299.

Garfinkel, C. I., T. A. Shaw, D. L. Hartmann, and D. W. Waugh, 2012: Does the Holton-Tan mechanism explain how the Quasi-Biennial Oscillation modulates the Arctic polar vortex? *J. Atmos. Sci.*, **69**, 1713–1733.

Garfinkel, C. I., D. W. Waugh, and E. P. Gerber, 2013: The effect of tropospheric jet latitude on coupling between the stratospheric polar vortex and the troposphere. *J. Clim.*, **26**, 2077–2095.

Garfinkel, C. I., I. P. White, E. P. Gerber, M. Jucker, and M. Erez, 2019: The building blocks of northern hemisphere wintertime stationary waves. *J. Clim.*, **Submitted**.

Gerber, E. P., and L. P. Polvani, 2009: Stratosphere-troposphere coupling in a relatively simple AGCM: The importance of stratospheric variability. *J. Clim.*, **22**, 1920–1933.

Gerber, E. P., and Coauthors, 2010: Stratosphere-troposphere coupling and annular mode variability in chemistry-climate models. *J. Geophys. Res. Atmos.*, **115**.

Haigh, J. D., M. Blackburn, and R. Day, 2005: The response of tropospheric circulation to perturbations in lower-stratospheric temperature. *J. Clim.*, **18**, 3672–3685.

Harnik, N., 2002: The evolution of a stratospheric wave packet. *J. Atmos. Sci.*, **59**, 202–217.

Hartley, D. E., J. T. Villarin, R. X. Black, and C. A. Davis, 1998: A new perspective on the dynamical link between the stratosphere and troposphere. *Nature*, **391**, 471–474.

Haynes, P. H., C. J. Marks, M. E. McIntyre, T. G. Shepherd, and K. P. Shine, 1991: On the ”downward control” of extratropical diabatic circulations by eddy-induced mean zonal forces. *J. Atmos. Sci.*, **48**, 651–678.

Held, I. M., and M. J. Suarez, 1994: A proposal for the intercomparison of the dynamical cores of atmospheric general circulation models. *Bull. Amer. Meteor. Soc.*, **75**, 1825–1830.

Hitchcock, P., and P. H. Haynes, 2016: Stratospheric control of planetary waves. *Geophys. Res. Lett.*, **43**, 11 884–11 892.

Hitchcock, P., T. G. Shepherd, and G. L. Manney, 2013: Statistical characterization of arctic polar-night jet oscillation events. *J. Atmos. Sci.*, **26**, 20962116.

Hitchcock, P., and I. R. Simpson, 2014: The downward influence of stratospheric sudden warmings. *J. Atmos. Sci.*, **71**, 3856–3876.

Hitchcock, P., and I. R. Simpson, 2016: Quantifying eddy feedbacks and forcings in the tropospheric response to stratospheric sudden warmings. *J. Atmos. Sci.*, **73**, 3641–3657.

Hoskins, B. J., and D. J. Karoly, 1981: The steady linear response of a spherical atmosphere to thermal and orographic forcing. *J. Atmos. Sci.*, **38**, 1179–1196.

Hoskins, B. J., and P. J. Valdes, 1990: On the existence of storm-tracks. *J. Atmos. Sci.*, **47**, 1854–1864.

Iacono, M. J., E. J. Mlawer, S. A. Clough, and J. J. Morcrette, 2000: Impact of an improved longwave radiation model, RRTM, on the energy budget and thermodynamic properties of the NCAR community climate model, CCM3. *J. Geophys. Res.*, **105**, 14 873–14 890.

Jucker, M., S. Fueglistaler, and G. K. Vallis, 2013: Maintenance of the stratospheric structure in an idealized general circulation model. *J. Atmos. Sci.*, **70**, 3341–3358.

Jucker, M., and E. P. Gerber, 2017: Untangling the annual cycle of the tropical tropopause layer with an idealized moist model. *J. Clim.*, **30**, 7339–7358.

Karpechko, A. Y., P. Hitchcock, D. H. W. Peters, and A. Schneidereit, 2017: Predictability of downward propagation of major sudden stratospheric warmings. *Q. J. R. Meteorol. Soc.*, **143**, 1459–1470.

Kidston, J., A. A. Scaife, S. C. Hardiman, D. M. Mitchell, N. Butchart, M. P. Baldwin, and L. J. Gray, 2015: Stratospheric influence on tropospheric jet streams, storm tracks and surface weather. *Nat. Geos.*, **8**, 433–440.

Kuroda, Y., and K. Kodera, 2001: Variability of the polar night jet in the northern and southern hemispheres. *J. Geophys. Res.*, **106**, 20 703–20 713.

Kushner, P. J., and L. M. Polvani, 2004: Stratosphere-troposphere coupling in a relatively simple agcm: The role of eddies. *J. Clim.*, **17**, 629–639.

Limpasuvan, V., D. W. Thompson, and D. L. Hartmann, 2004: The life cycle of the northern hemisphere sudden stratospheric warmings. *J. Clim.*, **17**, 2584–2596.

Lorenz, D. J., and E. T. DeWeaver, 2007: Tropopause height and zonal wind response to global warming in the IPCC scenario integrations. *J. Geophys. Res.*, **112**.

Martineau, P., S.-W. Son, M. Taguchi, and A. H. Butler, 2018: A comparison of the momentum budget in reanalysis datasets during sudden stratospheric warming events. *Atmos. Chem. and Phys.*, **18 (10)**, 7169–7187, doi:10.5194/acp-18-7169-2018, URL https://www.atmos-chem-phys.net/18/7169/2018/.

Matsuno, T., 1970: Vertical propagation of stationary planetary waves in winter northern hemisphere. *J. Atmos. Sci.*, **27**, 871–883.

Matsuno, T., 1971: A dynamical model of the stratospheric sudden warming. *J. Atmos. Sci.*, **28**, 1479–1494.

Maycock, A. C., and P. Hitchcock, 2015: Do split and displacement sudden stratospheric warmings have different annular mode signatures? *Geophys. Res. Lett.*, **42**, 10 943–10 951.

McInturff, R. M. E., 1978: Stratospheric warmings: Synoptic, dynamic and general-circulation aspects. Tech. Rep. NASA Reference Publ. NASARP-1017, Nat. Aeronautics and Space Admin., Goddard Space Flight Cent.

Mlawer, E. J., S. J. Taubman, P. D. Brown, M. J. Iacono, and S. A. Clough, 1997: Radiative transfer for inhomogeneous atmospheres: RRTM, a validated correlated-k model for the longwave. *J. Geophys. Res.*, **102**, 16 663–16 682.

Nakagawa, K. I., and K. Yamazaki, 2006: What kind of stratospheric sudden warming propagates to the troposphere? *Geophys. Res. Lett.*, **33 (L04801)**.

Perlwitz, J., and N. Harnik, 2003: Observational evidence of a stratospheric influence on the troposphere by planetary wave reflection. *J. Clim.*, **16 (18)**, 3011–3026.

Plumb, R. A., and K. Semeniuk, 2003: Downward migration of extratropical zonal wind anomalies. *J. Geophys. Res.*, **108 (D7)**.

Polvani, L. M., and P. Kushner, 2002: Tropospheric response to stratospheric perturbations in a relatively simple general circulation model. *Geophys. Res. Lett.*, **29 (7)**.

Polvani, L. M., and D. W. Waugh, 2004: Upward wave activity flux as a precursor to extreme stratospheric events and subsequent anomalous surface weather regimes. *J. Clim.*, **17 (18)**, 3548–3554.

Rao, J., Y. Y. Yu, D. Guo, C. H. Shi, D. Chen, and D. Z. Hu., 2019: Evaluating the brewer-dobson circulation and its reponses to enso, qbo, and the solar cycle in different reanalyses. *Earth Planet Phys.*, **3 (2)**, 1–16.

Robinson, W. A., 2000: A baroclinic mechanism for the eddy feedback on the zonal index. *J. Atmos. Sci.*, **57**, 415–422.

Scherhag, R., 1952: Die explosionsartigen stratosphrenerwrmungen des sptwinter 1951/1952 (the explosive warmings in the stratosphere of the late winter 1951/1952). *Ber. Dtsch. Wetterdienstes U.S. Zone*, **38**, 51–63.

Shaw, T. A., J. Perlwitz, and N. Harnik, 2010: Downward wave coupling between the stratosphere and troposphere: The importance of meridional wave guiding and comparison with zonal-mean coupling. *J. Clim.*, **23**, 6365–6381.

Shepherd, T. G., K. Semeniuk, and J. N. Koshyk, 1996: Sponge layer feedbacks in middle-atmosphere models. *J. Geophys. Res.*, **101**, 23 447–23 964.

Shepherd, T. G., and T. A. Shaw, 2004: The angular momentum constraint on climate sensitivity and downward influence in the middle atmosphere. *J. Atmos. Sci.*, **61**, 28992908.

Sheshadri, A., R. A. Plumb, and E. P. Gerber, 2017: Propagating annular modes: Empirical orthogonal functions, principal oscillation patterns, and time scales. *J. Atmos. Sci.*, **74**, 1345–1361.

Sigmond, M., J. F. Scinocca, V. V. Kharin, and T. G. Shepherd, 2013: Enhanced seasonal forecast skill following stratospheric sudden warmings. *Nat. Geosci.*, **6**, 98–102.

Simpson, I. R., P. Hitchcock, T. G. Shepherd, and J. F. Scinocca, 2011: Stratospheric variability and tropospheric annular-mode timescales. *Geophys. Res. Lett.*, **38**.

Simpson, I. R., B. M., and J. D. Haigh, 2009: The role of eddies in driving the tropospheric response to stratospheric heating perturbations. *J. Atmos. Sci.*, **66**, 1347–1365.

Smith, K. L., and R. K. Scott, 2016: The role of planetary waves in the tropospheric jet response to stratospheric cooling. *Geophys. Res. Lett.*, **43**, 2904–2911.

Song, Y., and W. Robinson, 2004: Dynamical mechanisms for stratospheric influences on the troposphere. *J. Atmos. Sci.*, **61**, 1711–1725.

Taguchi, M., T. Yamaga, and S. Yoden, 2001: Internal variability of the tropospherestratosphere coupled system simulated in a simple global circulation model. *J. Atmos. Sci.*, **58**, 3184–3203.

Thompson, D. W. J., J. C. Furtado, and T. G. Shepherd, 2006: On the tropospheric response to anomalous stratospheric wave drag and radiative heating. *J. Atmos. Sci.*, **63**, 2616–2629.

White, I. P., C. G. Garfinkel, E. P. Gerber, M. Jucker, V. A. Aquila, and L. D. Oman, 2019: The downward influence of sudden stratospheric warmings: association with tropospheric precursors. *J. Clim.*, **32**, 85–108.

Williams, G. P., 2006: Circulation sensitivity to tropopause height. *J. Atmos. Sci.*, **63**, 1954–1961.

# LIST OF FIGURES

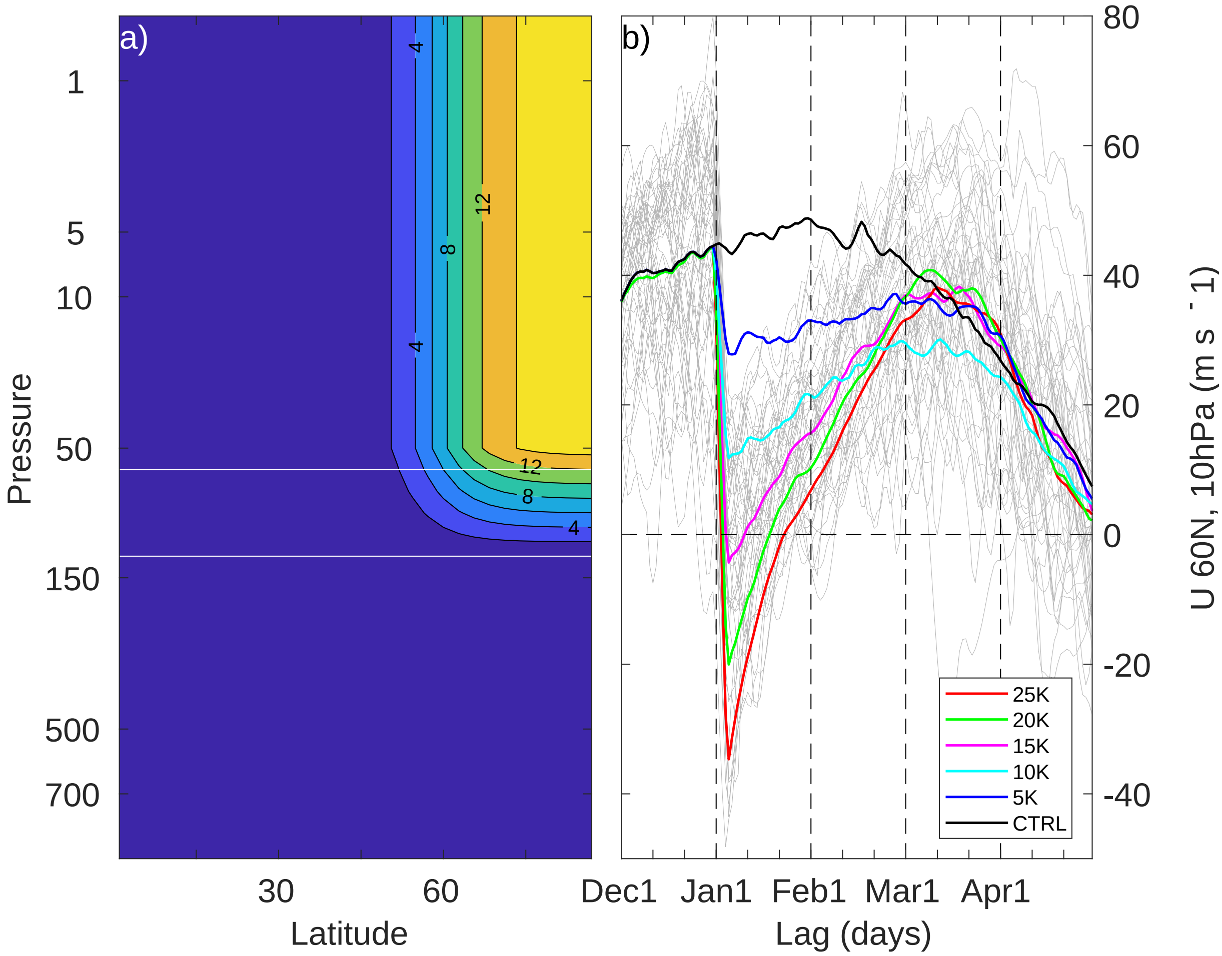


FIG. 1. (a) Idealised thermal-forcing profile with $Q = 15\mathrm{Kday}^{-1}$. The two horizontal lines indicate the region where the forcing linearly drops off between $p_t = 60$ hPa and $p_b = 150$ hPa. All other parameters are as in section 2b. (b) Timeseries from December 1st to May 1st of the ensemble-mean $\overline{u}$ at 60°N, 10 hPa for each of the five PTRB experiments and CTRL. Thin grey lines indicate the evolution for all 50 ensemble members in the 15-K PTRB experiment.

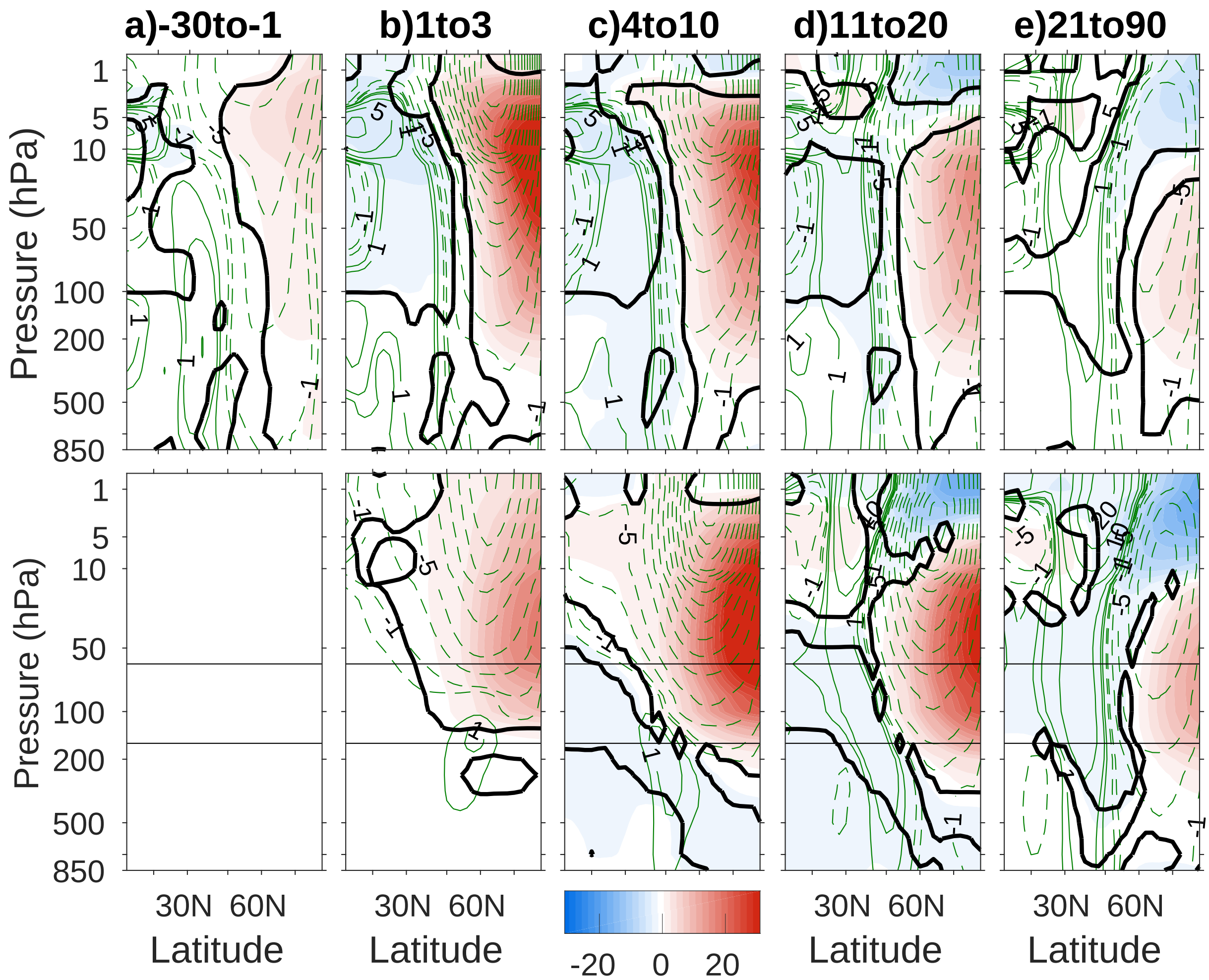


FIG. 2. (Top row): Latitude-height cross-sections of the $\overline{T}$ (shading; units: $K$) and $\overline{u}$ (green contours; units: $ms^{-1}$) ensemble-mean SSW anomalies averaged over different lag stages in CTRL. Solid (dashed) green contours represent positive (negative) $\overline{u}$ anomalies with contours at $\pm 0.5, 1, 2.5, 5, 10, \ldots ms^{-1}$. Thick black line indicates statistically significant $\overline{T}$ anomalies from the climatology in CTRL. (Bottom Row): Same as top row except for the 15-K PTRB experiment. Note that the lags for the PTRB experiments are according to the start of the thermal forcing stage (January 1st). Thin horizontal lines are as in figure 1a.

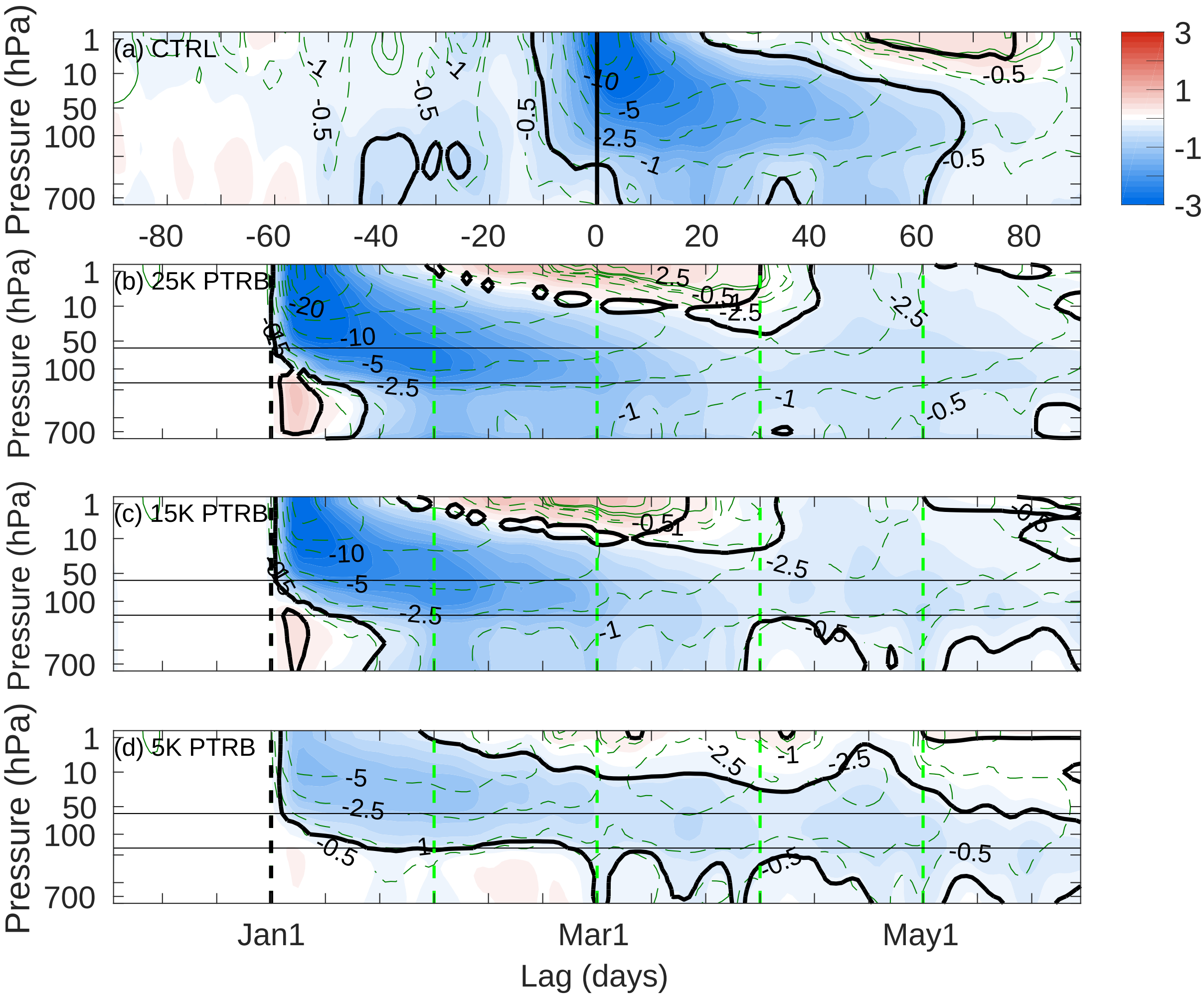


FIG. 3. Height-lag composites of the NAM index (shading with units of standard deviations) averaged over 60-87°N and over all SSWs in the CTRL run (a), 25-K (b), 15-K (c) and 5-K (d) PTRB experiments. The green contours show $\overline{u}$ anomalies averaged over 60-80°N with the same contour spacing as in figure 2. Dashed black vertical lines indicate the SSW onset in (a) and January 1st in (b-c), whereas dashed green lines in (b-c) represent the first of each month. Note therefore that lag 0 in (a) should be matched with January 1st in (b-d).

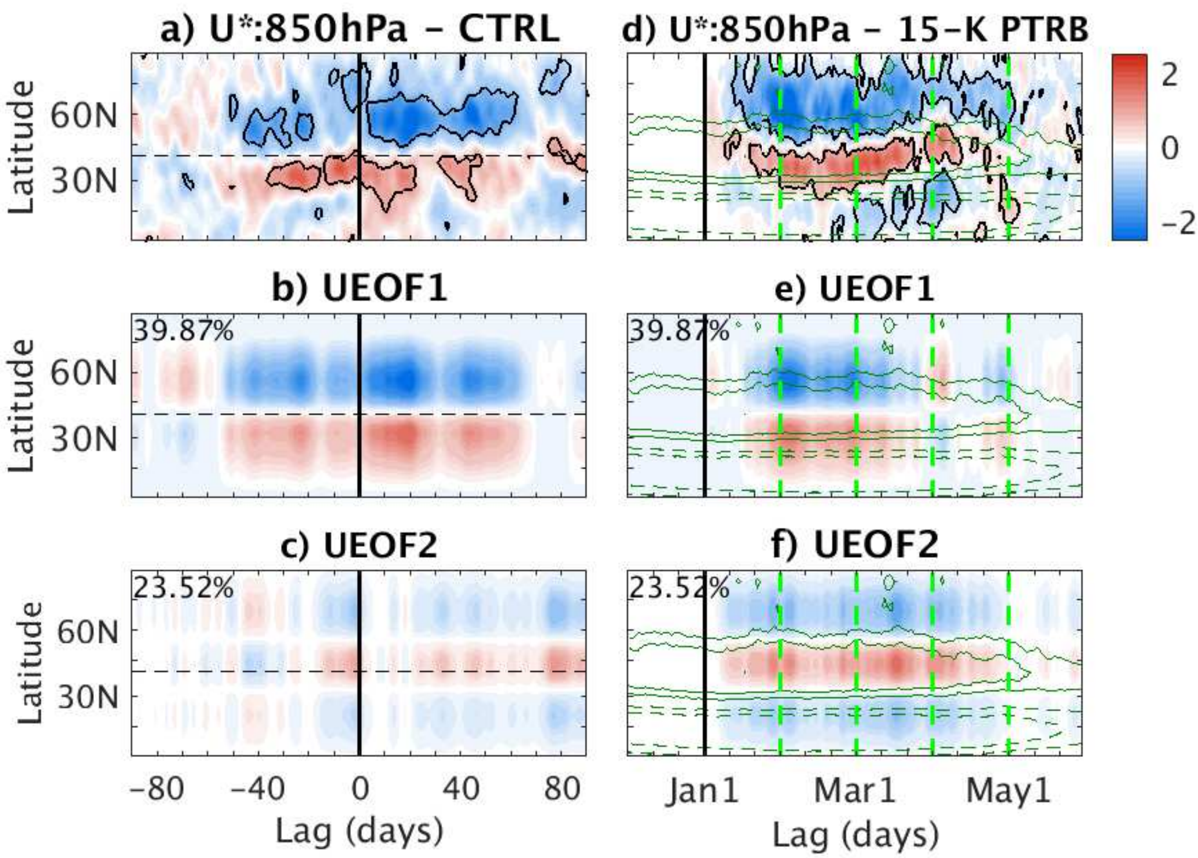


FIG. 4. (Top Row): Latitude-lag composites of $\overline{u}$ anomalies at 850 hPa for the CTRL SSWs (a) and the 15-K PTRB SSWs (b). (Middle Row): Projection of $\overline{u}$ anomalies from the top row onto the first EOF of the CTRL run. Horizontal line indicates the December-February climatological $\overline{u}$ in CTRL. (Bottom Row): Same as middle except as a projection onto the second EOF. Green contours in the right column indicate the daily climatological $\overline{u}$ at this level with values at $\pm$2.5,5,10,...ms$^{-1}$. Vertical lines as in figure 3.

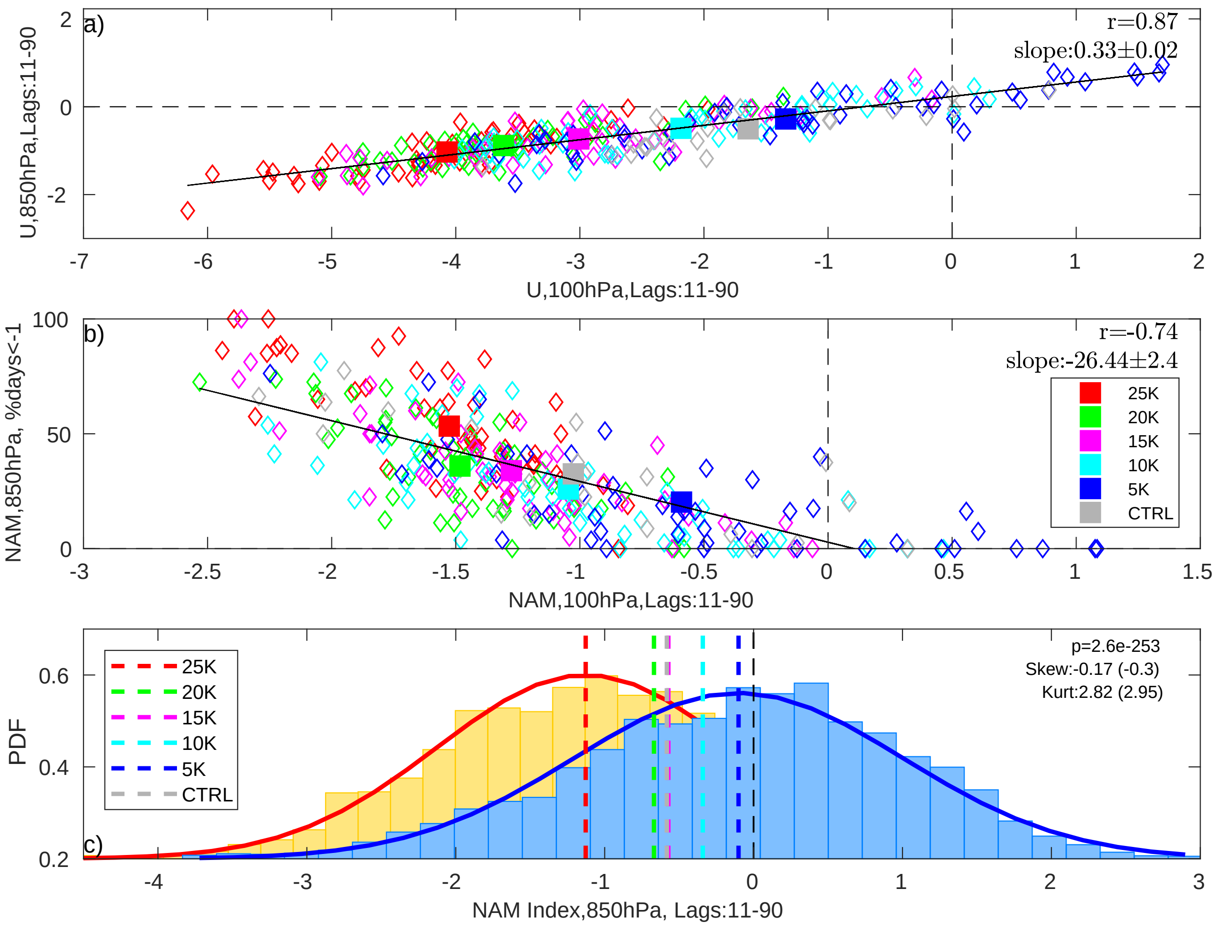


FIG. 5. (a) Scatter plot of $\overline{u}$ at 100 hPa against $\overline{u}$ at 850 hPa, both averaged over 60-87N and lags 11-90, for five PTRB experiments (see legend) and CTRL. Filled coloured squares indicate the corresponding ensemble means for each experiment. (b) Scatter plot of the NAM index at 100 hPa averaged over lags 11-60, against the percentage of days post-onset, that the NAM at 850 hPa is smaller than a threshold of one standard deviation. Black lines show the line of best fit calculated using a least-squares fit. The slope of the linear regression lines (along with the confidence intervals) and the correlation coefficients ($r$) are included in the top right of both (a) and (b). (c) Histograms of the daily NAM index at 850 hPa for positive lags for the 25-K PTRB (orange/red) and the 5-K PTRB (blue). The Kolgomorov-Smirnov test is used to test the siginficance between the two histograms with the p-value shown in the top right corner of (b). Also shown in the top right are the skewness and kurtosis for the two histograms with the 5-K PTRB values in parentheses. Coloured dashed vertical lines represent the ensemble means for each PTRB experiment (including the remaining three PTRB experiments as well as for CTRL).

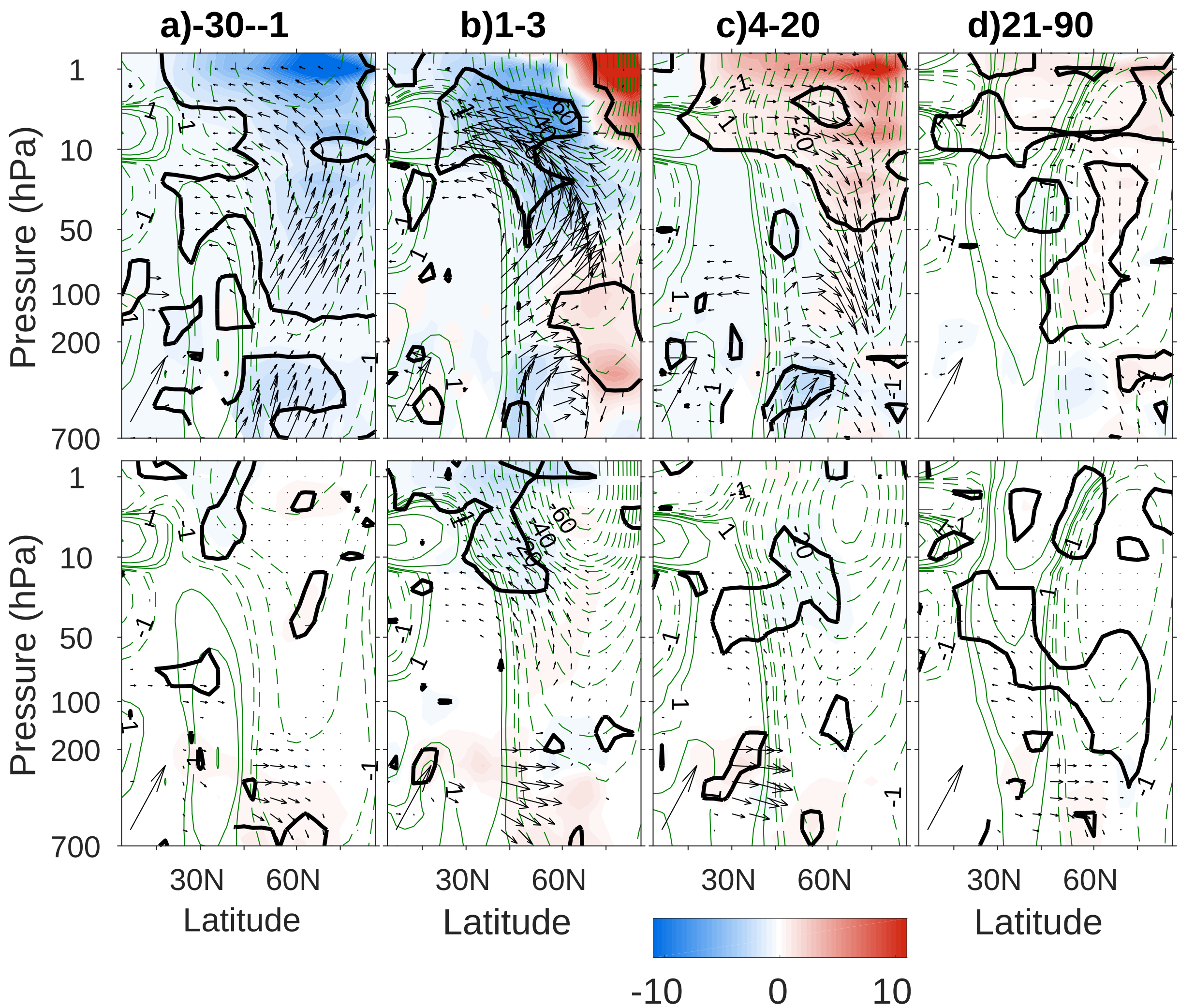


FIG. 6. Latitude-height cross-sections of the Eliassen-Palm flux (**F**; arrows) and the Eliassen-Palm flux divergence term ($\Pi = \nabla \cdot \mathbf{F}/\rho_0 a \cos\varphi$; shading) anomalies averaged over various lag stages, and filtered for planetary waves 1-3 (top) and synoptic waves 4+ (bottom). A lower level of 700 hPa is used here to avoid complications with topography when calculating the eddy contributions to **F** in equations (5) and (6). Stratospheric arrows are scaled by a factor of 5 to aid in visualisation. Units of $\Pi$ is m s$^{-1}$ day$^{-1}$. Thin green contours and thick black contour as in figure 2. Note that only **F** vectors for which either one of its components is statistically significant are plotted. Lag stages averaged over are indicated at the top of each column.

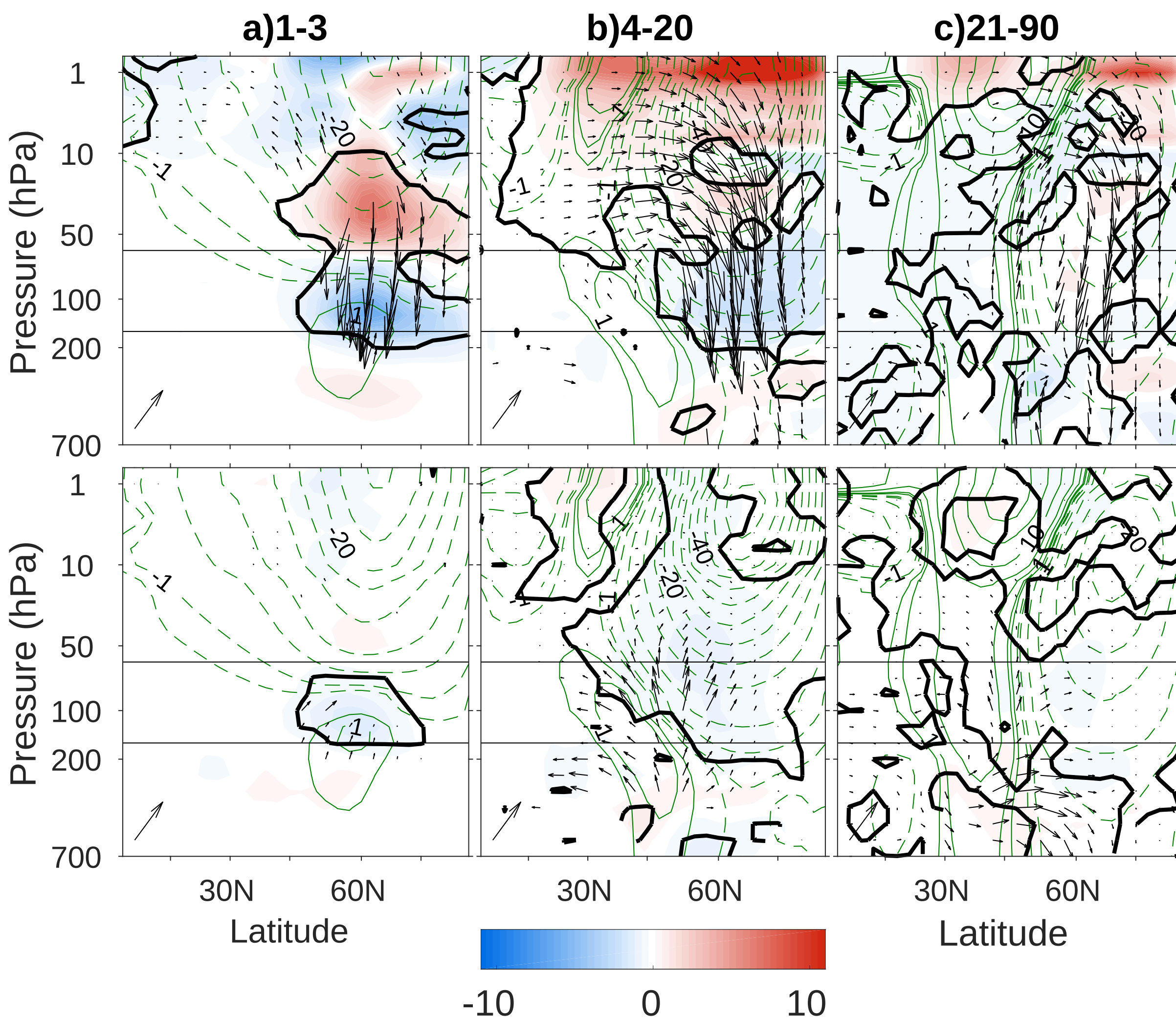


1051 FIG. 7. As in figure 6 except for the 15-K PTRB and with the omission of the panels at negative lags. Thin
1052 horizontal lines as in Figure 1b.

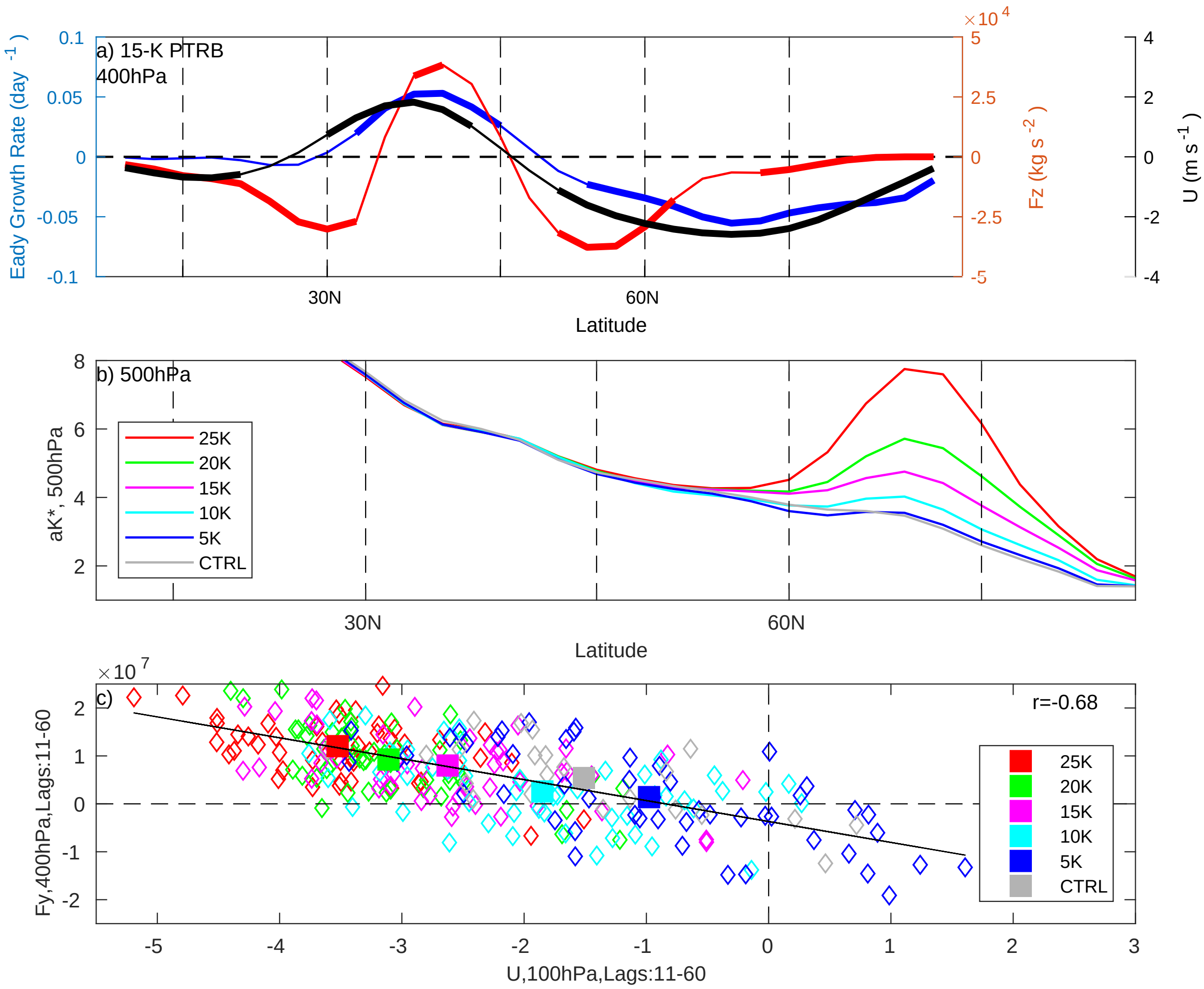


1053 FIG. 8. (a) Latitudinal profile of the Eady growth rate $\sigma$ (blue line; units of day$^{-1}$), synoptic-wave $F^{(z)}$ (red
1054 line) and $\overline{u}$ (black line) anomalies at 400 hPa and averaged over lags 21-90 for the 15-K PTRB. Double-thickness
1055 lines indicate statistically-significant differences from CTRL at the 95% level. (b) Latitudinal profiles of the total
1056 wavenumber $K^*$ (with $c = 0$ and multiplied by the Earth's radius) at 500 hPa for all PTRB experiments 15-K
1057 PTRB experiment (solid blue line). The DJF climatological $aK^*$ for CTRL is also plotted in grey. (c) Scatter
1058 plot of $\overline{u}$ at 100 hPa and averaged over 60-87°N and lags 11-60 (units: m s$^{-1}$), against the synoptic-wave $F^{(\varphi)}$
1059 at 400 hPa, averaged over 45-55N and over lags 11-60. Correlation coefficient is included in top right of (c).

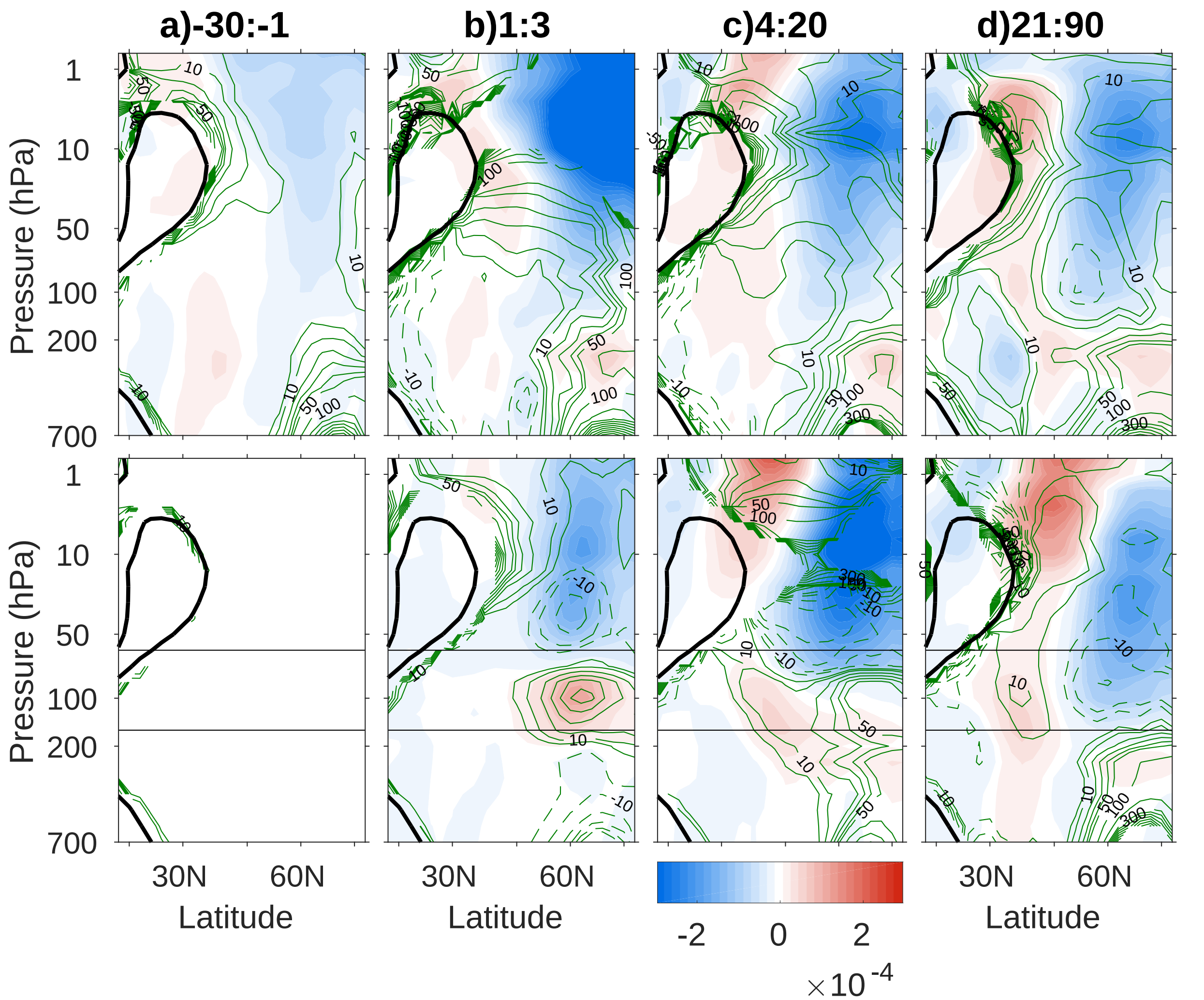


FIG. 9. Quasi-geostrophic refractive index ($n^2$; contours) and potential vorticity gradient ($\overline{q}_\varphi$; shading) anomalies averaged over various lag stages for CTRL (top) and the 15-K PTRB experiment (bottom). Solid (dashed) green contours indicate positive (negative) $n^2$ anomalies. Note that $n^2$ has been scaled by $a^2$ and is hence dimensionless, whereas $\overline{q}_\varphi$ has units of $s^{-1}$. Contours of $n^2$ are at $\pm 100, 200, \ldots, 1000$ with additional contours at $\pm 5, 10, 20, \ldots, 50$. Also, note that $n^2$ contours have been omitted where $\overline{u} < 0$ (N.B. that $\overline{u}$ in this case is the full field and not the anomaly). See text for details regarding the calculations for both CTRL and PTRB. Thick black line is the December to February climatological zero-wind line. Horizontal lines in the bottom row are as in figure 1b.

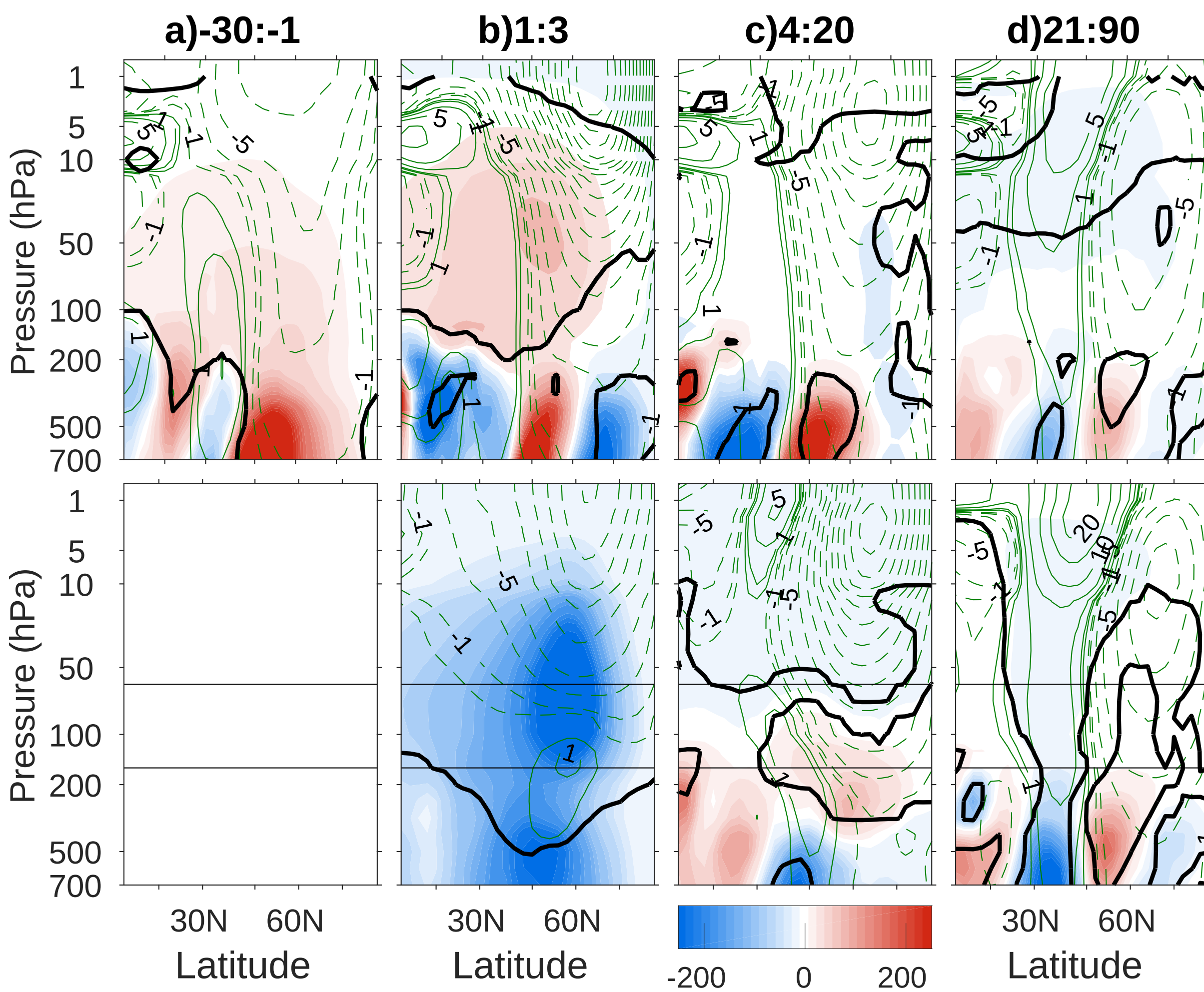


FIG. 10. Latitude-height cross-sections of the residual mean meridional circulation $\Psi^*$ (units of kg m s$^{-2}$), averaged over lags (a) -30–1, (b) 1-3, (c) 4-20, and (d) 21-90 for the CTRL (top row) and 15-K PTRB experiment (bottom row). Note that the two lag stages 4-10 and 11-20 in figure 2 have been averaged into a single panel here, for brevity. Green contours represent the corresponding $\overline{u}$ anomalies at these lags with contours at $\pm 0.5, 1, 2.5, 5, 10, \ldots$m s$^{-1}$. Thick black (grey) contour indicates statistical significance at the 95% (90%) level with the latter being added in contrast to other figures to make clear the significant regions.